Accepted Manuscript

Influence of porosity parameters and electrolyte chemical composition on the power densities of non-aqueous and ionic liquid based supercapacitors

R. Härmas, R. Palm, M. Härmas, M. Pohl, H. Kurig, I. Tallo, E. Tee, I. Vaas, R. Väli, T. Romann, O. Oll, R. Kanarbik, K. Liivand, J. Eskusson, J. Kruusma, T. Thomberg, A. Jänes, P. Miidla, E. Lust

PII: S0013-4686(18)31403-8

DOI: 10.1016/j.electacta.2018.06.115

Reference: EA 32108

To appear in: *Electrochimica Acta*

Received Date: 3 February 2018

Revised Date: 13 June 2018

Accepted Date: 16 June 2018

Please cite this article as: R. Härmas, R. Palm, M. Härmas, M. Pohl, H. Kurig, I. Tallo, E. Tee, I. Vaas, R. Väli, T. Romann, O. Oll, R. Kanarbik, K. Liivand, J. Eskusson, J. Kruusma, T. Thomberg, A. Jänes, P. Miidla, E. Lust, Influence of porosity parameters and electrolyte chemical composition on the power densities of non-aqueous and ionic liquid based supercapacitors, *Electrochimica Acta* (2018), doi: 10.1016/j.electacta.2018.06.115.

This is a PDF file of an unedited manuscript that has been accepted for publication. As a service to our customers we are providing this early version of the manuscript. The manuscript will undergo copyediting, typesetting, and review of the resulting proof before it is published in its final form. Please note that during the production process errors may be discovered which could affect the content, and all legal disclaimers that apply to the journal pertain.

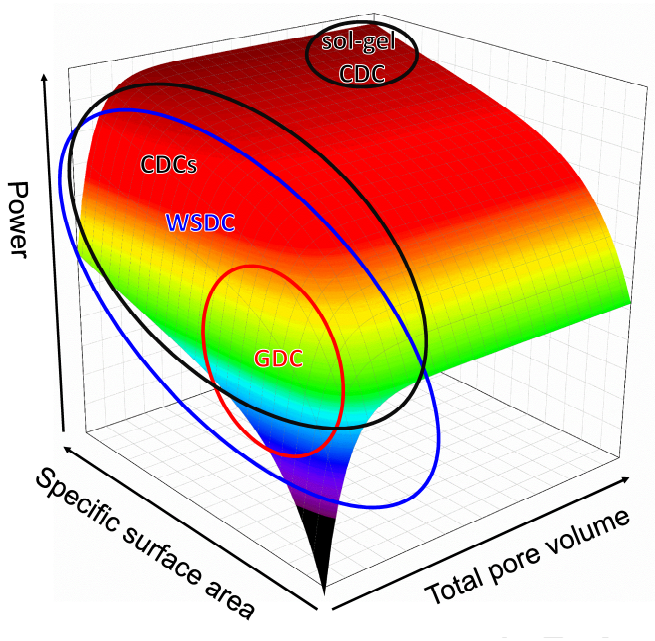

ACCEPTED MANUSCRIPT

ACCEPTED MANUSCRIPT

Influence of porosity parameters and electrolyte chemical composition on the power densities of non-aqueous and ionic liquid based supercapacitors

R. Härmas[a], R. Palm[a], M. Härmas[a], M. Pohl[a], H. Kurig[a,1], I. Tallo[a], E. Tee[a], I. Vaas[a], R. Väli[a,1], T. Romann[a,1], O. Oll[a,1], R. Kanarbik[a], K. Liivand[a], J. Eskusson[a], J. Kruusma[a], T. Thomberg[a,1], A. Jänes[a,1], P. Miidla[b], E. Lust[a,1*]

[a]*Institute of Chemistry, University of Tartu, Ravila 14a, 50411 Tartu, Estonia*

[b]*Institute of Mathematics and Statistics, J. Liivi 2, 50409 Tartu, Estonia*

Abstract

Influence of specific surface area (S_{DFT}), total pore volume (V_{tot}) and other porosity characteristics on the electrochemical parameters and power density of two electrode electric double layer capacitors based on 1 M 3-ethyl-methylammonium tetrafluoroborate (Et_3MeNBF_4) solution in acetonitrile and on 1-ethyl-3-methylimidazolium tetrafluoroborate ($EtMeImBF_4$) has been analysed. The pore size distribution data calculated from nitrogen, CO_2 and Ar adsorption isotherms using mainly Carbon 2D non-local density functional theory for heterogeneous surface (2D-NLDFT-HS) model have been compared with crystallographic characteristics obtained by Raman, X-ray diffraction, photoelectron spectroscopy, etc. methods. It was shown that, chemical composition and crystallographic structure of precursor material, synthesis and activation

*Corresponding author. Tel.: + 372 737 5165; fax: + 372 737 5264; e-mail: enn.lust@ut.ee
[1]ISE member.

conditions have decisive influence on the shape (spherical, cylindrical or slit-shape pores) and hierarchical porous structure and electrical conductivity of the carbon materials. Noticeable increase in series and parallel capacitances from 50 to 138 F g^{-1} in 1 M Et_3MeNBF_4 and up to 155 F g^{-1} in $EtMeImBF_4$, gravimetric power density (up to 35 kW kg^{-1}) and volumetric power density (up to 25 kW dm^{-3}, both at discharge time 3.6 s in 1 M Et_3MeNBF_4 + AN electrolyte) for optimised EDLC has been demonstrated. For $EtMeImBF_4$ based cells lower gravimetric (25 kW kg^{-1}) and volumetric (10 kW dm^{-3}) power densities have been achieved. For completing the EDLCs with high power and energy densities, highly micro-and mesoporous materials with optimum specific surface area (1200 – 1500 m^2 g^{-1}) but maximum (meso) pore volume (V_{tot} > 1.5 cm^3 g^{-1}) should be applied. Only for optimized EDLCs the very short characteristic charging/discharging times (lower than 0.3 s in Et_3MeNBF_4 + AN and 1.0 s in $EtMeImBF_4$) can be achieved.

Keywords: porous carbon; non-aqueous and ionic liquid based electrolyte; supercapacitor; gravimetric and volumetric energy and power densities

1. Introduction

Disordered carbons are widely used for modern energy conversion/storage devices. Carbon materials with high surface area and microporous/mesoporous structure are effectively used for electrical double layer supercapacitors (EDLC) [1–10]. However, the same carbons do not perform well in Li- or Na-ion batteries and polymer electrolyte fuel cells (PEMFC) [10–15]. The highest power densities have been established for PEMFC electrodes based on mesoporous carbon derived from Mo_2C [10-13]. In batteries, high

energy densities have been established for graphite (Li-ion batteries) or partially graphitized disordered carbons, e.g. carbon nanospheres based electrodes synthesized from D-glucose or white sugar (Na-ion batteries) [14,15]. Also, the performance of PEMFC improves when carbon materials with larger extent of mesopores and optimum level of graphitization (good electrical conductivity) are used as electrode materials. In addition, Pt-nanoclusters activated electrodes prepared from Mo_2C, VC, WC, TiC and α-SiC derived carbon materials have demonstrated long-lasting durability and higher power densities compared with Vulcan or other amorphous carbons based electrodes [11–13]. The porosity characteristics (specific surface area, ratio of microporous/mesoporous volumes), electrical conductivity and graphitization level depend heavily upon the precursor material and the preparation and activation method of a carbon material used [1–33]. Various disordered carbons synthesized from biomass (coconut shells, beat, sugar/crane residuals, coffee bean wastes), carbides, sugar, etc. have been used for preparation of the electrodes for different but moderate energy storage/conversion devices (EDLC, PEMFC, Na- and Li-ion batteries) [1–6,10,14–16,29,32,33].

In the optimisation process of porous electrodes different aspects, like the Debye screening length of solvated ions (increasing with dilution of electrolyte) and its dependence on the electric field strength (decreasing with the electric field strength) should be considered in order to develop high power/ energy density devices with excellent performance and time-stability [1–6,16,18–42]. Influence of the chemical composition and solvation energy of an electrolyte (Et_3MeNBF_4, Et_4NBF_4, Et_4NClO_4, $LiClO_4$, $NaClO_4$, $LiBF_4$, $LiClO_4$, $LiPF_6$, $NaPF_6$, $LiCF_3SO_3$ or caesium carborane in various organic solvents (Et = ethyl and Me = methyl)) on EDLC performance has been

analysed systematically [18–37,43]. It has been found that non-aqueous electrolytes with concentration lower than 1 M cannot be used for completing a high energy/power density EDLC. Electrochemical behaviour of novel doubly charged cations [38] and substituted phosphonium cations [39] in non-aqueous solvents have also been tested, but moderate energy/power densities have been calculated. Applicability limits of CDC, D-glucose and white sugar derived activated carbons have been established in different electrolytes.

Electrochemical characteristics of carbon materials in pure ionic liquids ($EtMeImBF_4$, $EtMeImB(CN)_4$, $EtMeImClO_4$, etc. (Im = imidazolium)) [40–46], their mixtures ($EtMeImBF_4$ + EtMeImI, $BuMeImBF_4$ + $EtMeImBF_4$) [47,48] and $EtMeImBF_4$ solutions in various solvents [41,49,50] have been obtained using electrochemical impedance spectroscopy, Fourier Transform Infrared spectroscopy (FTIR) [51,52] and *operando* ultra-high vacuum synchrotron-radiation X-ray photoemission spectroscopy (SR XPS) [53–56]. Ideal polarizability limits and mechanisms of possible faradic reactions (including electro-polymerization at high negative potentials and fluorination reactions at high positive potentials) have been established [51–56].

Strong influence of the carbon precursor materials (carbide, D-glucose, white sugar, organic aerogel), synthesis parameters (chlorination temperature of carbides, pyrolysis and hydrothermal carbonization temperature and pressure) and activation conditions (applying CO_2, H_2O, KOH, $ZnCl_2$ and combined KOH + $ZnCl_2$ activators) of carbon powders on the characteristics of EDLC containing room temperature ionic liquids (RTIL) or RTIL mixtures has been demonstrated [9,57–61].

In this paper, the data for hierarchical microporous/mesoporous carbons with widely variable porous structure derived from binary and ternary carbides (CDC), TiC

prepared by sol-gel method, hydrothermally carbonized glucose (GDC) and white sugar (WSDC) [7–10,17–33] will be discussed in the light of novel data from small angle neutron scattering [17], *in situ*/ *operando* XPS and SR-XPS [53–56] and FTIR methods [51,52]. Systematic analysis of N_2, Ar, and CO_2 adsorption data will be given. Well-expressed dependences of series capacitance, characteristic time constant, gravimetric and volumetric power and energy densities on the specific surface area, pore volume and hierarchical porous structure, established using nitrogen, argon and carbon dioxide adsorption methods, and on the crystallographic ordering of carbon powders, demonstrated by small angle neutron scattering (SANS) and high-resolution transmission electron microscopy (HR-TEM) methods, will be analyzed.

2. Experimental

2.1. Synthesis of microporous and micro-mesoporous carbon powders

Our discussion covers EDLCs based on carbon powders obtained by chlorination of binary and ternary carbides [22,24,31,62] and TiC prepared by sol-gel method [33], as well as by hydrothermal carbonization of D-glucose (GDC) [32,46] and white sugar (WSDC) solutions [58].

TiC, α-WC, VC, Mo_2C, α-SiC, Ta_4HfC_5 and $WTiC_2$ (Alfa Aesar, USA) have been used for the preparation of carbide derived carbon (CDC) powders [7,8,19–27,30,31,33]. A carbide was held in a flow of Cl_2 (99.99%, Linde Gas (AGA)) at a fixed temperature ranging from 600 to 1100 °C for the reaction between the carbide and Cl_2 (α-SiC, WC, VC, TiC at 600 – 1100 °C, Mo_2C-CDC at 600–1200 °C). Resulting carbons are noted as X-CDC Y in the text, where X denotes the precursor carbide and Y denotes the synthesis

temperature in Celsius degrees. For analysis of the influence of the reactant composition and the preparation conditions on the carbon characteristics, HCl instead of Cl_2 has been used for preparation of some carbons (TiC-CDC 700–1100) [30]. Some CDC powders were further activated with CO_2 (AGA, purity 99.99%) for 3 h at 950 °C [57].

After chlorination and CDC activation the CDC powder was treated with H_2 at 800 or 900 °C in order to remove residues of chlorine and all possible functional groups from the CDC surface [17–22,30–33].

Sol-gel synthesis process was applied to obtain titanium carbide and titanium carbide/carbon nanotubes composites. All resulting materials were pyrolyzed, chlorinated at 950 °C and thereafter reduced with H_2 at 900 °C for 1.5 h [33].

Carbonaceous powders were prepared from D-(+)-glucose (Sigma Aldrich GmbH) (GDC) and white sugar (WSDC) by the hydrothermal carbonization method. GDC was subsequently activated with $ZnCl_2$, KOH, or a mixture of $ZnCl_2$ and KOH (GDC:$ZnCl_2$:KOH) [32] or pyrolyzed and activated with CO_2 (GDC-CO_2) [28,46]. WSDC was activated chemically with $ZnCl_2$ [58]. All resulting carbon powders were reduced with H_2 at 800 °C for 2 h [32,46,58]. For comparison, some data for microporous carbon fabrics (SvetlogorskKhimvolokno, Belarus) [63] have also been used in analysis.

2.2. Carbon characterization

2.2.1. Gas adsorption measurements

N_2, Ar and CO_2 sorption measurements of carbon powders at 77 K, 87 K and 283 K, respectively, have been conducted on ASAP 2020 (Micromeritics) and 3Flex (Micromeritics, USA) systems. The 2D non-local density functional theory based on

heterogeneous carbon surface model (2D-NLDFT HS) implemented in SAIEUS software (Micromeritics) [64] has been used to calculate the specific surface area (S_{DFT}), pore volume (V_{DFT}) and pore size distribution data. For comparison, other NLDFT models (Standard Slit; Aspect Ratio 4, 6 and 8) implemented in SAIEUS software [64] and also traditional Brunauer-Emmett-Teller multipoint theory (denoted as S_{BET}) [65] have been used. The total volume of pores (V_{tot}) and the volume of micropores (V_{micro}) (as well as mesopores (V_{meso}) from the difference between V_{tot} and V_{micro}) have been calculated using the *t*-plot method [66]. The detailed analysis of methods used for porosity analysis is given in Härmas et al. [67].

2.2.2. Physical characterization methods

The transmission electron microscopy (TEM) and HRTEM, (Tecnai G20 FEI instrument operating at the 200 kV accelerating voltage) and scanning electron microscopy (SEM, Zeiss EVO MA15 equipped with Oxford X-Max 80 mm 2 energy dispersive X-ray spectrometer) have been used for imaging the structure and chemical composition of carbon powders. In addition, selected area electron diffraction (SAED) and electron energy loss spectroscopy (EELS) have been applied for structural and chemical analysis of powders [24,30–33,45].

In order to estimate the overall atomic composition of functional groups at the carbon surface, the secondary ion mass spectroscopy (SIMS), XPS and X-ray fluorescence spectroscopy (XRF) measurements were conducted using a surface station equipped with an electron energy analyser (SCIENTA SES 100) and a non-monochromatic twin anode X-ray tube (Thermo XR3E2). For some materials (Mo_2C-

CDC) *operando* synchrotron radiation (SR) beam based ultra-high vacuum SR XPS has been used (MaxLab II I411 beam, Lund) [53–56,68].

Raman spectroscopy measurements were conducted on inVia micro-Raman spectrometer (Renishaw) with excitation wavelength 514 nm. *In situ* FTIR was performed using a Perkin Elmer Spectrum GX FTIR equipped with a liquid nitrogen-cooled mid-range MCT detector [51,52]. The band fitting of first order Raman spectra was carried out with OriginPro 2016 software (OriginLab). The SANS method has been used for analysis of the pore shape of carbons prepared from a-SiC, TiC and Mo_2C [17]. The detailed method of fitting is described by Härmas et al. [67].

2.3. Electrochemical cells and electrochemical analysis methods

2.3.1. Preparation of EDLC electrodes

The carbon film (thickness 100 ± 5 μm) was prepared from synthesized carbon powder with 6 wt% of polytetrafluoroethylene (PTFE) addition and roll pressed (HS-160 N, Hohsen Corp.) at 20 ± 1 °C [9,16–33]. After drying under vacuum (10^{-9} Torr) a pure Al (99.99%) layer (thickness of 2 μm) was deposited onto one side of the electrode by magnetron sputtering method. After that, the electrodes were transported into the glove box using a special Ar-filled transport vessel to avoid any contact with oxygen and other electrochemically active compounds after high-vacuum treatment step.

For non-aqueous and RTIL based EDLC measurements, the standard Al test cell (HS TestCell, Hohsen Corp.) with two identical electrodes (flat cross-section area of 2.0 cm^2) was completed inside a glove box (LabMaster sp, MBRAUN; O_2 and H_2O concentrations lower than 0.1 ppm) [39,40,43,45–50]. The carefully dried (at 80 ^oC,

reduced pressure) 25 μm thick TF4425 separator (Nippon Kodoshi, Japan) was used for mechanical separation of the working electrodes. Electrochemical tests were carried out mainly at T = 20 ± 1 °C, but some EDLC cells were tested within wide T region from –40 °C to 80 °C (mixtures of ionic liquids with organic electrolytes, non-aqueous electrolytes with specific additives, etc.) [40,42,50].

2.3.2. Electrochemical characterization of a single cell

EDLCs have been studied using cyclic voltammetry (CV) at scanning rates from 1 mV s^{-1} to 1 V s^{-1}, constant current charge/discharge (CCCD) from 0.2 to 10 A g^{-1} and electrochemical impedance spectroscopy (EIS, frequency range from 1 mHz to 300 kHz, 5 mV *ac* modulation) methods using SI 1287 Solartron potentiostat and 1252A frequency response analyser and/or Parstat MC 1000 (Princeton Applied Research, USA). Constant power tests have been performed on a BT2000 testing system (Arbin Instruments, USA). The general measurement setup has been described elsewhere [30–32]. The series capacitance, C_s, and parallel capacitance, C_p, have been calculated from Nyquist plots measured at fixed cell potentials using Eq. 1 and Eq. 2, respectively:

$$C_s(\omega) = \frac{-1}{\omega Z''(\omega)} \quad (1)$$

$$C_p(\omega) = C_s(\omega)[1 + \tan^2(\frac{-Z'(\omega)}{Z''(\omega)})], \quad (2)$$

where $Z'(\omega)$ and $Z''(\omega)$ are the real and imaginary parts of the impedance, respectively, and ω is the angular frequency. $C_s(\omega)$ has been analyzed in a complex form:

$$C_s(\omega) = C'(\omega) - iC''(\omega), \quad (3)$$

where the real part $C'(\omega)$ and imaginary part $C''(\omega)$ of capacitance are:

$$C'(\omega) = \frac{-Z''(\omega)}{\omega|Z(\omega)|^2}, \qquad C''(\omega) = \frac{-Z'(\omega)}{\omega|Z(\omega)|^2}, \tag{4}$$

and $|Z(\omega)|$ denotes the impedance modulus. The low frequency part of $C'(\omega)$ corresponds to the so called static capacitance, which is measured during the constant discharge. $C''(\omega)$ corresponds to the energy dissipation of the capacitance $C_s(\omega)$, i.e. an irreversible process which can lead to the hysteresis of the electrochemical process [1,69]. The $C''(\omega)$ vs. ac frequency (f) dependence has a maximum at the so-called relaxation frequency, f_R, which determines the time constant, $\tau_R = (2\pi f_R)^{-1}$.

The ideal double layer capacitive behaviour (i.e. potential region, where the role of faradaic processes is negligible) has been established from the shape of the log($-Z''$) vs. log$f$ plots [22–34,70] (slope values more negative than –0.98; for ideal EDLC –1.0) as well as Bode phase angle vs. log$f$ plots, accepting that for EDLC the phase angle $\delta \leq -88°$ (for an ideal capacitive system $\delta = -90°$). For systematic analysis of the capacitance data, only the potential region, where the $C_s(\omega)$ and $C_p(\omega)$ values overlap at $\omega \rightarrow 0$ (i.e. free of the contribution of faradic reactions) has been used.

The complex power is expressed as:

$$S(\omega) = P(\omega) + iQ(\omega), \tag{5}$$

where the real part $P(\omega)$ is:

$$P(\omega) = \omega\, C''(\omega)|\Delta V_{\mathrm{rms}}|^2, \tag{6}$$

and the imaginary part $Q(\omega)$ is:

$$Q(\omega) = -\omega\, C'(\omega)|\Delta V_{\mathrm{rms}}|^2, \tag{7}$$

where $|\Delta V_{\mathrm{rms}}|^2 = \frac{\Delta V_{\mathrm{max}}}{\sqrt{2}}$, and V_{max} is the maximum amplitude of *ac* voltage applied [1,3,7–9,69]. An ideal capacitor (i.e. a system with ideal capacitive behaviour) has no real part, as there is only a reactive contribution to the complex power [68]:

$$S(\omega) = \mathrm{i}Q = -\frac{\mathrm{i}\Delta \mathrm{V}_{\mathrm{rms}}^2}{|Z''|}. \quad (9)$$

Systems with ideal resistive behaviour (ideal resistance) have no imaginary part as this component only dissipates energy and the complex power takes the well-known form:

$$S(\omega) = \frac{\Delta \mathrm{V}_{\mathrm{rms}}^2}{|Z'|} \quad (10)$$

It would be noted that real EDLCs oscillate between the two states mentioned before: resistive at high frequencies ($\omega \rightarrow \infty$) and capacitive at low frequencies ($\omega \rightarrow 0$). Between these two states, the EDLC behaves like a resistance-capacitance (RC) transmission-line circuit [61–63,68–70].

3. Results and discussion

3.1. Physical characterization

3.1.1. Gas adsorption data and applicability of pore shape models

The shape of adsorption isotherm of a carbon powder depends noticeably on the precursor material used (Fig. 1). Carbons prepared from organic aerogels and Mo_2C at temperatures higher than 700 °C and TiC-CDC prepared at 1100 °C contain both micro- and mesopores, i.e. are the micro-mesoporous materials as the hysteresis loops are clearly visible in their isotherms (Fig. 1). Carbons synthesized from TiC, α-WC, α-SiC, VC, Mo_2C (synthesis $T \leq 700$ °C) and D-glucose are mostly microporous (no hysteresis loops in the N_2 sorption isotherms). The comparison of adsorption isotherms (Fig. 2) (and more

data in Härmas et al. [67]) shows that the amount of gas adsorbed (so-called cumulative pore volume) depends remarkably on the gas used (N_2, CO_2, Ar) as well as on the material tested (Figs. 1 and 2). However, it should be noted that N_2 and Ar adsorption takes place at $T \leq 87$ K, but CO_2 adsorption at 273 K, where the energy of heat fluctuations is remarkably higher. Similar complicated behaviour has been discussed by many authors [71–73]. However, more detailed mathematical analysis is inevitable for overwhelming conclusions.

The pore size distribution plots (Fig. 3) have been calculated based on the CO_2, N_2 and Ar adsorption isotherms using 2D-NLDFT HS model [64]. For microporous materials reduced with H_2, the pore size distribution plots overlap roughly and there is no dependence of the peak position on the gas used (demonstrated in Fig. 3a). For non-reduced microporous SiC-CDC (Fig. 3b), the position of the peaks in the pore size distribution plots depends slightly on the gas used, indicating that there might be specific adsorption of the gases on the functionalized surface [71–73]. For very well reduced micro-mesoporous material, the peak positions in the pore size distribution plots depend weakly on the gas used (not shown for shortness).

Evidently, the shape of adsorption isotherms (Fig. 4a) and the peak positions in the pore size distribution plots for CDC (Fig. 4b) also depend on the type of the NLDFT model (Heterogeneous Surface; Aspect Ratio 4, 6 and 8; Standard Slit) used for fitting of the calculated isotherms to the experimental ones and thus also on the pore geometry assumed [17,71–75]. Consequently, for the detailed analysis of the pore size distribution data the pore shape (geometry) should be established using X-ray and/or neutron tomography, HRTEM, SAXS , SANS [17,70,71] or other methods in order to have an

independent verification of the carbon structure and, thus, physical evidence to support the choice of the NLDFT model. However, HRTEM, EELS and SAED data for various carbon materials (Figs. 5 and 6) show, that there are graphitized areas at carbon powder surface (slit-shaped pores) and amorphous areas inside the carbon particles (mainly having a cylinder or sphere like shape or combinations of spherical, cylindrical and/or slit-shaped pores). These data are in an agreement with SANS data demonstrating that in SiC-CDC 1000 there are mainly spherical pores, in TiC-CDC 950 cylindrical and in Mo2C-CDC 1000 the slit shape pores prevail [17,74,75].

In conclusion, HRTEM, FIB-SEM, TOF-SIMS (FIB – focused ion beam, TOF – time of flight) and X-ray tomography data [75] confirm that there are different pores with variable shape and linear dimensions expressed at surface layers and in porous volume of carbon materials. The isotherms of mostly microporous carbons (TiC-CDC-900 and 700, all SiC-CDC materials) can be fitted reasonably well with the Heterogeneous Surface model (2D-NLDFT HS, [64]) (Figs. 1, 3 and 4). This model fits also the data for micro-mesoporous materials with hierarchical bi-modal pore size distribution (Mo_2C-CDC 900 and 1000, TiC-CDC 1100, WC-CDC 1100) (Figs. 1–4) better than the other models (Standard Slit, Aspect ratio 4,6 and 8). However, for well-expressed hierarchical micro-mesoporous materials (Mo2C-CDC 900, 1000 and 1100) there is no ideal fit because the bimodal pore size distribution and energetic inhomogeneity of Mo_2C-CDC powder surface (sp^2 and sp^3 electronic states, discussed in next chapter) generates variations in adsorption energies and this effect has not been taken fully into account in the NLDFT models applied [64,71,72]. Thus, future developments of the NLDFT models taking into account the differences in adsorption energies, caused by energetic (sp^2 and sp^3 electronic

configurations) and crystallographic ((0001), higher index planes, amorphous areas) inhomogeneities of surfaces, are inevitable.

3.1.2. Results of physical characterisation methods

In order to determine the general correlations between gas adsorption and electrochemical impedance data for various electrodes it is necessary to apply additional independent methods for obtaining the crystalline and energetic (sp^2, sp^3) characteristics of carbon powders.

A selection of XRD data for carbons under study is given in Figs. 5 and 6. It is clearly visible that the crystallinity of the carbon material depends on the precursor chemical composition and on the synthesis temperature applied. In the diffractograms for carbide-derived carbons prepared at higher temperatures (Mo_2C-CDC 1000, TiC-CDC 1050 and 1100, WC-CDC 1100, etc.), the reflections (002) and (100)/(101) are clearly seen (Fig. 5d). For the CDCs synthesised at lower temperatures ($T \leq 800$ °C), the (002) and (100)/(101) reflections are lacking (Figs. 5a, 6a, 6c, 6d). Thus, CDCs synthesized at higher temperatures are more ordered and crystalline. Crystallite size (L_a) values for some CDCs, calculated from the XRD diffractograms with Scherrer equation (detailed description is given in Härmas et al. [67]), are given in Fig. 5b. It is clearly seen, that the ordered crystalline areas in powders grow in size as the synthesis temperature of carbons increases.

XRD data for GDC [32,46] and WSDC [58] show lower crystallinity compared with CDCs prepared at comparable synthesis temperatures. Organic aerogel derived carbons (OADC) are mainly amorphous [29].

XRD data are in a good agreement with HRTEM results (Figs. 5c and d) demonstrating that the surfaces of Mo_2C-CDC 1000 (Fig. 7a), TiC-CDC 1050 and WC-CDC 1100 (Fig. 5d) are very well ordered and a few layer thick curved graphitic areas can be seen. Selected area electron diffraction (SAED) data also confirm the existence of graphitic domains on the surface of these carbons (Fig. 5d). Electron energy loss spectroscopy (EELS) data, given in Figs. 5c and 5d (insets) show peaks characteristic of π*- and σ-bonds, which indicate the existence of both sp^2 and sp^3 structural areas in WC-CDC 1100 (it is also the case for Mo_2C-CDC 1000, data not shown for shortness). However, π*-peaks, which characterize existence of widely graphitized regions, are not seen in the EELS spectra for all carbons synthesized at temperatures below 800 °C (Fig. 6c). Despite the presence of widely graphitized regions in carbons prepared at $T \geq$ 1000 °C (Mo_2C-CDC, TiC-CDC, etc.), the HRTEM data show that even in these CDC carbons the amorphous regions are still present inside the particles (Figs. 5c, 5d and 7a).

Operando ultra-high vacuum SR XPS data also show two type of carbon regions with sp^2 and sp^3 electronic states, respectively (Fig. 7b) [53–56]. In the case of carbons reduced with hydrogen at 800 °C and thereafter keeped in Ar-filled vessel, no remarkable oxygen functionalities have been observed on the electrode surfaces. This result is in a very good agreement with the SIMS, XPS, XRF and SEM-EDX data (not shown for shortness). However, different oxygen containing functional groups have been observed at non-reduced carbon surfaces in agreement with thermogravimetry data (not shown for shortness). Oxygen containing functional groups on carbon surface can interact with CO_2 and/or nitrogen during the respective gas sorption measurements and therefore an overestimated specific surface areas and pore volumes can be calculated. The SIMS,

XPS, XRF and SEM-EDX data additionally prove that the materials can be cleaned from Cl_2 and chlorine based contaminants using the H_2 cleaning step.

Hence, the raw material used, the synthesis method and temperature and also activation methods influence on the crystallographic ordering of the carbon structure, increasing with treatment temperature [2–10,16–33].

3.1.3. Analysis of Raman spectroscopy data

The shape and intensity of the Raman spectra are also strongly influenced by the synthesis method and temperature applied for preparation of the carbon powders (Figs. 8a–8d and more detail analysis is given in Härmas et al. [67]), analysing characteristics of WC-CDC, Mo_2C-CDC and α-SiC-CDC 1100 prepared at different activation times from 0 to 12h). In the first order Raman excitation region there are two clearly exposed well-known peaks— the G and D peaks originating from the ordered graphite-like areas, and the edges of the ordered areas (i.e. from defects), respectively [76]. The most common parameter used to characterize the Raman spectrum of a disordered carbon is the intensity of the D-peak divided by the intensity of the G-peak [9,22,24,31,77–80]. However, there is some confusion connected with interpretation/calculation of this parameter [77–93]. More detailed explanations how the Raman data have been analysed is given in Ref. [67] and only very brief discussion is given here.

In the case of disordered carbons, many authors have used more than two peaks to fit the calculated spectrum to the first order region experimental Raman spectrum [83-86], however there is no consensus of the physical meaning of these extra peaks or how many and which type of fitting functions should be used [76,79,86–89].

Based on the analysis of fitting results of many Raman spectra for our carbons we finally decided to fit the spectrum with two Lorentzian and two Gaussian functions since this approach yields the best fitting of experimental results (more detailed analysis and discussion is given in Ref. [67]). To clarify, which parameter obtainable from the Raman spectrum is suitable to characterize the crystallinity of CDCs, the plots of I_D/I_G, I_{Df}/I_{Gf}, $FWHM_D$ [90], $FWHM_G$, S'_D/S'_G vs. synthesis temperature (T_{syn}) (Figs. 9a and 9b, and [67]) were constructed [86]. It should be noted that the $FWHM_D$ value is less sensitive to the method used for fitting the spectrum than the other Raman spectrum parameters (I_{Df}/I_{Gf}, $FWHM_G$, S'_D/S'_G) as the D-band is usually very strong and easy to fit in the first order Raman spectrum of disordered carbons [67,90,91]. A clear trend can be seen in the graph – the higher the T_{syn}, the narrower the D-peak (Fig. 9b).

The second order region of the disordered carbon Raman spectrum conveys information about the stacking of the graphene layers [92]. In an agreement with SR XPS, HRTEM and XRD results for some CDCs (Mo_2C-CDC) a well-developed 2D peak can be seen, which characterizes well-developed graphitization and stacking of sp^2 layers (Figs. 8a and 8d). For SiC-CDC 1100, GDC-CO_2 and TiC-CDC (Figs. 8b-8d) there is a second small peak at ~2980 cm^{-1}, sometimes denoted as 2G″ and explained as the superposition of D- and G-peaks. However, the origin of 2G″ peak is under debate at the moment [92,93].

3.2. Electrochemical characterization

3.2.1. Analysis of cyclic voltammetry and impedance data

The cyclic voltammetry (current density, i, vs. cell potential, ΔE) plots, measured at fixed potential scanning rates (v) from 1 mV s^{-1} to 1 V s^{-1}, have been recalculated into integral capacitance C_{CV} vs. ΔE plots (Fig. 10) using Eqs. 11 and 12:

$$C_{\mathrm{CV}} = \frac{\Delta q}{\Delta E} \tag{11}$$

$$\Delta q = \int_{\Delta E_1}^{\Delta E_2} i(\Delta E)\mathrm{d}t = \int_{\Delta E_1}^{\Delta E_2} i(\Delta E)\frac{\mathrm{d}(\Delta E)}{E} \tag{12}$$

For a symmetrical 2-electrode cell, the specific integral capacitance for one electrode is calculated using Eq. (13):

$$C_{\mathrm{m}} = \frac{2C_{\mathrm{CV}}}{m}, \tag{13}$$

where m is the mass of one electrode. The calculated C_m values are independent of v if v is lower than 100 mV s^{-1} [18–34,40,41,46–50]. Additionally, the capacitance values have been calculated from linear constant current charge/discharge plots (from 0.3 to 10 A g^{-1}) (C_{CC}) and from the impedance data (C_s) (Fig. 11) [18–34,40,41,46–50]. It has been found that there is a very good agreement between capacitance values calculated using different calculation methods (C_m, C_{CC} and C_s) [18–34,40,41,46–50], if v < 100 mVs^{-1}, charging current is lower than 2 A g^{-1} (thus, C_{CC} have been calculated only from linear CC plots) and *ac* frequency is lower than 0.1 Hz within the region of ideal polarizability, indicating that the equilibrium capacitance values have been obtained free from any faradic process contribution.

It is evident from Eq. 2, that, for ideal double layer systems (EDLC) [1,7–9] at low ac frequency, the C_s values overlap with C_p values (i.e. C_s, vs. log$f$ and C_p vs. log$f$ plots overlap, Fig. 11a). The condition C_s = C_p also points to equilibrium capacitance

[33]. These equilibrium $C_s(\omega\rightarrow 0) = C_p(\omega\rightarrow 0)$ values have been used for construction of the C_s vs. S_{DFT} and C_s vs. V_{DFT} plots (Fig. 12, Tables 1 and 2).

For systematic analysis of correlation between electrochemical data for EDLCs and gas phase adsorption data for carbon materials used to complete the EDLCs, the pores smaller than 0.7 nm have been eliminated from calculations of S_{DFT} and V_{DFT} [6,94–98] (description of the procedure is given in [67]) because these small pores are assumed to be inaccessible to accumulate the solvated or desolvated ions (diameter ≈ 0.7 nm for Et_3MeN^+) [6,20,94–96]. This approximation has been used for better comparison of our data with the results published by other groups [95–98]. Thus, in this article S_{DFT} and V_{DFT} denote the surface area and volume of pores with widths wider than 0.7 nm (Table 2) [6,94,95]. It should be noted that this approximation is bit oversimplified because the effective diameter of ions, i.e. effective Debye screening length decreases with the electric field strength (cell potential (Fig. 10a)). In addition, the effective surface roughness of electrodes increases with the cell potential applied [6-9,18–41]. Therefore, the Gibbs adsorption of ions probably increases with the cell potential expressed as a very slow increase of capacitance with increasing the electric field strength (cell potential) [6-8,18–41]. However, it should be noted that all general correlations established (Figs. 12a–12c) are also valid in the case of application of the total (non-corrected) $S_{DFT,tot}$ and $V_{DFT,tot}$ values (data and discussion in [67]).

Data in Figs. 12a – c show the logarithmic (asymptotic) dependences of C_s on S_{DFT} and on V_{DFT}. In addition, also the dependences of C_s on S_{micro}, V_{micro}, S_{meso} and V_{meso} have been constructed but more expressed deviation of the data for microporous electrodes based EDLCs from general correlations has been observed.

It is interesting that all well-developed micro- and/or micro-mesoporous CDC, GDC, WSDC, and sol-gel method TiC derived carbons scale up to nearly comparable capacitance values: 130 ± 20 F g^{-1} for Et_3MeNBF_4 + acetonitrile solution. The highest C_s (C_p) values have been calculated for partially graphitized micro- mesoporous Mo_2C-CDC and sol-gel TiC-CDC with slit shape porous structure and for additionally activated GDC and WSDC electrodes composed from nano-spherical particles [32,46,58]. Similar strong dependence of capacitance on the specific surface area has been discussed by other authors for non-aqueous [95,96,99–101] and H_2O + H_2SO_4 based systems [102–105]. Limiting capacitances for 1 M Et_3MeNBF_4 are somewhat lower (from 5 to 15%) than the capacitance values for single cells based on electrochemically stable ionic liquids: $Et_3MeImBF_4$ (up to 155 F g^{-1}) and $Et_3MeImB(CN)_4$ (150 F g^{-1}) [19]. The biggest outliers in the C_s vs. S_{DFT} and C_s vs. V_{DFT} plots (Figs. 12a and 12b) are EDLCs based on microporous amorphous α-SiC-CDC synthesized at 600, 700 and 800 °C [19,44] and microporous carbon electrodes (TiC-CDC 600, WC-CDC 900, VC-CDC 800 and very microporous carbon fabric), indicating that absence of the well-developed mesoporosity lowers the specific capacitance and, thus, the possible energy density (Eq. 14) of an EDLC.

Usually the theoretical energy densities (E_{max}) and power densities (P_{max}) have been calculated using Eqs. (14) and (15) and the corresponding so-called theoretical Ragone plots have been constructed [6–9,23-33,45–50]:

$$E_{max} = \frac{C_s\, S_{el}\, \Delta E^2}{2\, m\, 3.6}, \tag{14}$$

and

$$P_{\max} = \frac{\Delta E^2 \, S_{\mathrm{el}}}{4 \, R_{\mathrm{E}} \, m} \, . \tag{15}$$

In Eqs. (14) and (15), C_s (F cm^{-2}) is the series capacitance at $f = 1 \cdot 10^{-3}$ Hz, S_{el} is the cross-section surface area of the electrodes, m is the mass of two electrodes (g), R_E (Ω cm^2) is the high-frequency series resistance. It should be noted that systematic comparison of the theoretically calculated power densities with experimentally measured Ragone plots for many two-electrode cells shows that Eq. (15) gives overestimated power densities (from 1.5 to 4 times depending on the high-frequency series resistance of a cell, adsorption equilibrium constants of anions and cations (adsorption resistance), and mass transfer coefficients of ions in porous matrix (determining the mass transfer resistance)). For correct power density / energy density analysis, the experimental constant power tests, i.e. experimental Ragone plots for the two electrode cells should be measured and discussed [6–9,23-33,45–50]. It should be stressed that the E_{max} and P_{max} values cannot be correctly calculated from the data measured for the three-electrode cell setup, calculated and published in some papers.

3.2.2. Analysis of characteristic time constant values

Data in Figs. 13 and 14 show the characteristic time constants $\tau_{char} = (2\pi f_{char})^{-1}$, where f_{char} is characteristic relaxation frequency that corresponds to the frequency of the maximum in the $C''(\omega)$ vs. log$f$ curve as well as to the intersection point of the imaginary power vs. real power plots (according to Eqs. (3–7)) [9,18–33]. The τ_{char} values depend strongly on the electrolyte viscosity and on the characteristics of carbon (i.e. on porosity), increasing with the increase of electrolyte viscosity and decreasing with the decrease of the pore width. τ_{char} is very long for microporous electrodes with spherical and cylindrical

pores (SiC-CDC, TiC-CDC), but very short for highly mesoporous sol-gel derived TiC-CDC [33] (Figs. 14a–14c) or Mo_2C-CDC (800 – 1000) having slit-shape porous structure. Even shorter τ_{char} values have been calculated for organic aerogel-derived mesoporous carbons based single cells [29]. Reliable τ_{char} values cannot be calculated for ultramicroporous non-activated SiC-CDC because the adsorption equilibrium has not been established even at very low *ac* frequency ($f = 1 \cdot 10^{-3}$ Hz). Thus, ultra-microporous materials (non-activated SiC-CDC) cannot be used for moderate or high power density EDLCs [6–9]. However, ultramicroporous/microporous carbon powders are very interesting materials for hydrogen and CH_4 storage [106].

The τ_{char} vs. S_{DFT} and vs. V_{DFT} plots (Fig. 14) show that there are two groups of EDLCs. For GDC:$ZnCl_2$:KOH, VC-CDC, Mo_2C-CDC, $WTiC_2$-CDC, sol-gel TiC-CDC and Ta_4HfC_5-CDC, there is a nearly logarithmic dependence of τ_{char} on S_{DFT} or on V_{DFT} (S_{DTF} and V_{DFT} values are given in Table 2). For mainly microporous materials (GDC-CO_2, WC-CDC, SiC-CDC (additionally activated with CO_2), TiC-CDC and carbon fabric) there is no well-expressed dependence of τ_{char} on S_{DFT} (Fig. 14a).

3.2.3. Analysis of constant power discharge data

Dependence of experimental gravimetric power density *P* on energy density *E*, i.e. experimental Ragone plots for EDLCs with Et_3MeNBF_4 + acetonitrile (AN) solution are given in Fig. 15a. Based on these data, the *P* vs. S_{DFT} and *P* vs. V_{DFT} (Table 2) plots have been constructed. For systematic analysis, the power densities calculated at fixed discharge times 3.6 s ($P_{3.6s}$) and 0.36 s ($P_{0.36s}$) have been used (Figs. 15 b–f). Reasonable asymptotic dependence common for all materials under analysis can be seen (statistical

fitting parameters are given in Table 1). More noticeable deviation from the general correlation line (Fig. 15b) has been observed for some D-glucose and sol-gel method prepared TiC-CDC materials toward higher $P_{3.6s}$ and $P_{0.36s}$ values. For materials with highly developed mesoporosity (Figs. 2–4), very high $P_{3.6s}$ and $P_{0.36s}$ values have been measured (Figs. 15a–15d). Deviation toward lower power density has been observed for $WTiC_2$-CDC and SiC-CDC without CO_2 activation step, i.e. for materials with well-developed ultra-micropores, but with lacking mesopores (Fig. 3).

Based on the data in Figs. 15a–15d, the 3D graphs have been constructed and are given (Figs. 15e and 15f). Detailed explanations are given in [67]. It is clearly visible, that both $P_{3.6s}$ and $P_{0.36s}$ increase quickly with V_{DFT} and S_{DFT} within moderate S_{DFT} and V_{DFT} values. The power densities and characteristic time constant (discharge time) values for the EDLCs studied approach limiting values at high S_{DFT} and V_{DFT} values explained by limiting Gibbs adsorption values at high cell potentials (3.0 V). Noticeably higher limiting power values have been calculated at shorter discharge times (0.36 s), thus, at lower energy densities, demonstrating quick desorption of ions from well-developed mesoporous areas during discharging of EDLCs. At fixed 0.36 s, there is a big decrease in E (nearly 50 times) very well visible in Fig. 15a.

Volumetric power density vs. energy density plots are shown in Fig. 16a. It can be concluded that similarly to gravimetric power density vs. V_{DFT} and vs. S_{DFT} plots, a clear increase in $P_{0.36}$ with S_{DFT} or V_{DFT} can be seen (Figs. 16b and c). Thus, highly mesoporous materials with high specific surface area are needed to create energy storage devices with high power density (main advantage of EDLCs). Similarly to gravimetric

3D plots data in Fig. 16d show that for high volumetric power density EDLCs materials with specific surface area and total pore volume are inevitable to apply.

4. Conclusions

The power density of electrical double layer supercapacitor cells completed from the electrodes based on micro- and micro- mesoporous carbon materials with various hierarchical structure and density functional theory surface area from 1000 to 2000 m^2/g and total pore volume from 0.5 to 2.2 cm^3 g^{-1} has been systematically analysed. 1.0 M 3-ethyl-methylammonium tetrafluoroborate (Et_3MeNBF_4) solution in acetonitrile and 1-ethyl-3-methylimidazolium tetrafluoroborate ($EtMeImBF_4$) have been used as electrolytes. N_2, CO_2 and Ar adsorption isotherms, total pore volume (from 0.5 to 3.5 cm^3 g^{-1}), pore size distribution data (from 0.6 to 3.5 nm) have been calculated using Carbon 2D non-local density functional theory for heterogeneous surface model. The calculated parameters depend very noticeably on the raw carbide and synthesis conditions used. Adsorption data have been compared with Raman spectroscopy, X-ray diffraction, high resolution transmission electron microscopy combined with selected area electron diffraction and electron energy loss spectroscopy, *operando* synchrotron radiation beam based ultra-high vacuum X-ray photoelectron spectroscopy data. It was concluded that the carbons synthesised have very complicated structure and in addition to the well graphitized and layered sp^2 surfaces areas the inner regions of these materials are mainly amorphous. The thickness of graphitization region and the lateral dimensions (from 2.0 to 5.5 nm) of graphitic areas increase with the increasing the synthesis temperature.

Absence of contaminants (chlorides, chlorine, raw carbides, etc.) has been verified using XPS, XRF, FIB-TOF-SIMS, HR-TEM-EDX methods.

For fitting of the adsorption isotherms and, hence, for obtaining the porosity parameters like specific surface area (S_{DFT}), pore volume (V_{DFT}), and pore size distribution being important for performance of an electrical double layer capacitor, the Carbon 2D non-local density functional theory for heterogeneous surface (2D-NLDFT-HS) has been used and the data have been compared with other NLDFT models (Standard Slit, Aspect Ratio 4, 6 and 8). It has been shown that the suitability of a model depends clearly on the structural peculiarities of a carbon material studied (pore size and shape, graphitization level). 2D-NLDFT-HS model fits reasonably well the microporous as well as moderately graphitized carbons like Mo_2C-CDC synthesized at temperatures lower than 900°C. However, the development of the NLDFT models taking into account the differences in adsorption energies, caused by geometric and electronic (sp^2 or sp^3) inhomogeneity of surfaces, is inevitable in order to improve the fittings for highly non-homogeneous carbons. More detailed analysis is given in Härmas et al. [67].

Electrochemical characteristics like region of ideal polarizability (up to 3.0 V for Et_3MeNBF_4 + AN (acetonitrile) or 3.2 V for $EtMeImBF_4$)), limiting capacitance values (up to 138 F g^{-1} for Et_3MeNBF_4 + AN and 155 F g^{-1} for $EtMeImBF_4$), characteristic time constant values (shorter than 0.3 s for Et_3MeNBF_4 + AN and 1.0 s for $EtMeImBF_4$) of the cells have been measured using cyclic voltammetry, constant current charge/discharge and electrochemical impedance methods. General dependences of the electrochemical parameters on S_{DFT} and V_{DFT} over various carbon materials have been drawn. It has been verified that the capacitance C_s increases noticeably at moderate S_{DFT} and V_{DFT} values

(from 50 to 120 F g^{-1}), however, C_s scales up to limiting values (138 F g^{-1} for Et_3MeNBF_4 and 155 F g^{-1} for $EtMeImBF_4$) at high S_{DFT} and V_{DFT}, which has been explained by limiting Gibbs adsorption of ions at/inside porous structure of the carbon electrodes at high cell potentials.

Experimental Ragone plots (i.e. gravimetric power up to 35 kW kg^{-1} (at 3.6 s discharge time) and volumetric power up to 20 kW dm^{-3} (at 3.6 s discharge time) for Et_3MeNBF_4 + AN have been measured. For $EtMeImBF_4$ electrolyte based EDLC, somewhat lower power (25 kW kg^{-1} and 10 kW dm^{-3}) have been measured explained by higher viscosity compared to acetonitrile based electrolyte. Quick decrease in power densities has been demonstrated for EDLCs based on carbon materials with intermediate or low S_{DFT} and V_{DFT} values. Scaling up of power densities (as well as energy densities) at high S_{DFT} and V_{DFT} values (logarithmic dependence of P_{max} on S_{DFT} and V_{DFT}) has been explained by limiting Gibbs adsorption and limiting mass transfer rate of ions at/inside porous structure of the carbon electrodes at high cell potentials.

It has been shown that the ultra-microporous materials have very long characteristic relaxation times, (longer than 10 s for Et_3MeNBF_4 +AN) increasing quickly with viscosity of electrolyte used (15 s for $EtMeImBF_4$). For optimised EDLCs the characteristic times are shorter than 0.3 s or 1.0 s for Et_3MeNBF_4 + AN and $EtMeImBF_4$, respectively. Thus, ultra-microporous materials with low S_{DFT} and V_{DFT} values are inapplicable for high power and energy density supercapacitors due to very low gravimetric and volumetric capacitance values explained by the very slow establishment of the adsorption equilibrium, especially in viscous $EtMeImBF_4$ ionic liquid.

Acknowledgements

This work was supported by the EU through the European Regional Development Fund under projects TK117 (3.2.0101–0030), TK 141 (2014-2020.4.01.15-0011) and NAMUR (3.2.0304.12-0397), and Higher education specialisation stipends in smart specialisation growth areas 2014-2020.4.02.16-0026; by the Estonian Research Council (institutional research grants IUT20-13 and IUT20-57 and personal research grants PUT55 and PUT1033), European Spallation Source: Estonian Participation in ESS Instrument design, development and building and application for scientific research (SLOKT12026T and SLTKT16432T). This work has been also partially supported by Graduate School of Functional materials and technologies receiving funding from the European Regional Development Fund in University of Tartu, Estonia.

References

[1] B.E. Conway, Electrochemical supercapacitors: scientific fundamentals and technological applications, Springer, New York, 1999.

[2] P. Simon, Y. Gogotsi, Materials for electrochemical capacitors, Nat. Mater. 7 (2008) 845–854. doi:10.1038/nmat2297.

[3] A. Burke, M. Miller, The power capability of ultracapacitors and lithium batteries for electric and hybrid vehicle applications, J. Power Sources. 196 (2011) 514–522. doi:10.1016/j.jpowsour.2010.06.092.

[4] F. Beguin, E. Frackowiak, Supercapacitors: Materials, Systems and Applications, John Wiley & Sons, 2013.

[5] M. Salanne, B. Rotenberg, K. Naoi, K. Kaneko, P.-L. Taberna, C.P. Grey, B. Dunn, P. Simon, Efficient storage mechanisms for building better supercapacitors, Nat. Energy. 1 (2016) 16070. doi:10.1038/nenergy.2016.70.

[6] G. Salitra, A. Soffer, L. Eliad, Y. Cohen, D. Aurbach, Carbon Electrodes for Double-Layer Capacitors I. Relations Between Ion and Pore Dimensions, J. Electrochem. Soc. 147 (2000) 2486–2493.

[7] M. Arulepp, J. Leis, M. Lätt, F. Miller, K. Rumma, E. Lust, A.F. Burke, The advanced carbide-derived carbon based supercapacitor, J. Power Sources. 162 (2006) 1460–1466. doi:10.1016/j.jpowsour.2006.08.014.

[8] E. Lust, G. Nurk, A. Jänes, M. Arulepp, P. Nigu, P. Möller, S. Kallip, V. Sammelselg, Electrochemical properties of nanoporous carbon electrodes in various nonaqueous electrolytes, J. Solid State Electrochem. 7 (2003) 91–105. doi:10.1007/s10008-002-0316-1.

[9] E. Tee, I. Tallo, H. Kurig, T. Thomberg, A. Jänes, E. Lust, Huge enhancement of energy storage capacity and power density of supercapacitors based on the carbon dioxide activated microporous SiC-CDC, Electrochim. Acta. 161 (2015) 364–370. doi:10.1016/j.electacta.2015.02.106.

[10] E. Antolini, Carbon supports for low-temperature fuel cell catalysts, Appl. Catal. B Environ. 88 (2009) 1–24. doi:10.1016/j.apcatb.2008.09.030.

[11] P.E. Kasatkin, R. Jäger, E. Härk, P. Teppor, I. Tallo, U. Joost, K. Šmits, R. Kanarbik, E. Lust, Fe-N/C catalysts for oxygen reduction based on silicon carbide derived carbon, Electrochem. Commun. 80 (2017) 33–38. doi:10.1016/j.elecom.2017.05.001.

[12] R. Jäger, E. Härk, P.E. Kasatkin, E. Lust, Investigation of a Carbon-Supported Pt Electrode for Oxygen Reduction Reaction in 0.1M KOH Aqueous Solution, J. Electrochem. Soc. 161 (2014) F861–F867. doi:10.1149/2.0491409jes.

[13] S. Sepp, J. Nerut, K. Vaarmets, R. Kanarbik, I. Tallo, H. Kurig, E. Lust, Enhanced Stability of Novel Hierarchical Carbon Supports in PEMFC Application, ECS Trans. 75 (2016) 789–799. doi:10.1149/07514.0789ecst.

[14] J.-Y. Hwang, S.-T. Myung, Y.-K. Sun, Sodium-ion batteries: present and future, Chem. Soc. Rev. 46 (2017) 3529–3614. doi:10.1039/C6CS00776G.

[15] N. Nitta, F. Wu, J.T. Lee, G. Yushin, Li-ion battery materials: present and future, Mater. Today. 18 (2015) 252–264. doi:10.1016/j.mattod.2014.10.040.

[16] R. Väli, A. Jänes, T. Thomberg, E. Lust, D-Glucose Derived Nanospheric Hard Carbon Electrodes for Room-Temperature Sodium-Ion Batteries, J. Electrochem. Soc. 163 (2016) A1619–A1626. doi:10.1149/2.0771608jes.

[17] H. Kurig, M. Russina, I. Tallo, M. Siebenbürger, T. Romann, E. Lust, The suitability of infinite slit-shaped pore model to describe the pores in highly porous carbon materials, Carbon. 100 (2016) 617–624. doi:10.1016/j.carbon.2016.01.061.

[18] M. Eikerling, A.A. Kornyshev, E. Lust, Optimized Structure of Nanoporous Carbon-Based Double-Layer Capacitors, J. Electrochem. Soc. 152 (2005) E24–E33. doi:10.1149/1.1825379.

[19] E. Lust, A. Jänes, M. Arulepp, Influence of electrolyte characteristics on the electrochemical parameters of electrical double layer capacitors, J. Solid State Electrochem. 8 (2004) 488–496. doi:10.1007/s10008-003-0458-9.

ACCEPTED MANUSCRIPT

[20] A. Jänes, L. Permann, M. Arulepp, E. Lust, Electrochemical characteristics of nanoporous carbide-derived carbon materials in non-aqueous electrolyte solutions, Electrochem. Commun. 6 (2004) 313–318. doi:10.1016/j.elecom.2004.01.009.

[21] A. Jänes, T. Thomberg, E. Lust, Synthesis and characterisation of nanoporous carbide-derived carbon by chlorination of vanadium carbide, Carbon. 45 (2007) 2717–2722. doi:10.1016/j.carbon.2007.09.041.

[22] A. Jänes, T. Thomberg, H. Kurig, E. Lust, Nanoscale fine-tuning of porosity of carbide-derived carbon prepared from molybdenum carbide, Carbon. 47 (2009) 23–29. doi:10.1016/j.carbon.2008.07.010.

[23] T. Thomberg, A. Jänes, E. Lust, Energy and power performance of vanadium carbide derived carbon electrode materials for supercapacitors, J. Electroanal. Chem. 630 (2009) 55–62. doi:10.1016/j.jelechem.2009.02.015.

[24] I. Tallo, T. Thomberg, K. Kontturi, A. Jänes, E. Lust, Nanostructured carbide-derived carbon synthesized by chlorination of tungsten carbide, Carbon. 49 (2011) 4427–4433. doi:10.1016/j.carbon.2011.06.033.

[25] T. Thomberg, H. Kurig, A. Jänes, E. Lust, Mesoporous carbide-derived carbons prepared from different chromium carbides, Microporous Mesoporous Mater. 141 (2011) 88–93. doi:10.1016/j.micromeso.2010.11.006.

[26] I. Tallo, T. Thomberg, A. Jänes, E. Lust, Electrochemical behavior of α-tungsten carbide-derived carbon based electric double-layer capacitors, J. Electrochem. Soc. 159 (2012) A208–A213.

[27] T. Thomberg, A. Jänes, E. Lust, Energy and power performance of electrochemical double-layer capacitors based on molybdenum carbide derived

carbon, Electrochim. Acta. 55 (2010) 3138–3143. doi:10.1016/j.electacta.2010.01.075.

[28] T. Thomberg, T. Tooming, T. Romann, R. Palm, A. Jänes, E. Lust, High Power Density Supercapacitors Based on the Carbon Dioxide Activated D-Glucose Derived Carbon Electrodes and Acetonitrile Electrolyte, J. Electrochem. Soc. 160 (2013) A1834–A1841. doi:10.1149/2.091310jes.

[29] A. Laheäär, A.-L. Peikolainen, M. Koel, A. Jänes, E. Lust, Comparison of carbon aerogel and carbide-derived carbon as electrode materials for non-aqueous supercapacitors with high performance, J. Solid State Electrochem. 16 (2012) 2717–2722. doi:10.1007/s10008-012-1660-4.

[30] I. Tallo, T. Thomberg, H. Kurig, A. Jänes, K. Kontturi, E. Lust, Supercapacitors based on carbide-derived carbons synthesised using HCl and Cl_2 as reactants, J. Solid State Electrochem. 17 (2013) 19–28. doi:10.1007/s10008-012-1850-0.

[31] I. Tallo, T. Thomberg, H. Kurig, K. Kontturi, A. Jänes, E. Lust, Novel micromesoporous carbon materials synthesized from tantalum hafnium carbide and tungsten titanium carbide, Carbon. 67 (2014) 607–616. doi:10.1016/j.carbon.2013.10.034.

[32] M. Härmas, T. Thomberg, H. Kurig, T. Romann, A. Jänes, E. Lust, Microporous–mesoporous carbons for energy storage synthesized by activation of carbonaceous material by zinc chloride, potassium hydroxide or mixture of them, J. Power Sources. 326 (2016) 624–634. doi:10.1016/j.jpowsour.2016.04.038.

[33] M. Pohl, H. Kurig, I. Tallo, A. Jänes, E. Lust, Novel sol-gel synthesis route of carbide-derived carbon composites for very high power density supercapacitors, Chem. Eng. J. 320 (2017) 576–587. doi:10.1016/j.cej.2017.03.081.

[34] A. Jänes, E. Lust, Electrochemical characteristics of nanoporous carbide-derived carbon materials in various nonaqueous electrolyte solutions, J. Electrochem. Soc. 153 (2006) A113–A116. doi:10.1149/1.2135212.

[35] A. Laheäär, A. Jänes, E. Lust, Electrochemical properties of carbide-derived carbon electrodes in non-aqueous electrolytes based on different Li-salts, Electrochim. Acta. 56 (2011) 9048–9055. doi:10.1016/j.electacta.2011.05.126.

[36] A. Laheäär, A. Jänes, E. Lust, Lithium bis(oxalato)borate as an electrolyte for micromesoporous carbide-derived carbon based supercapacitors, J. Electroanal. Chem. 669 (2012) 67–72. doi:10.1016/j.jelechem.2012.01.025.

[37] A. Laheäär, A. Jänes, E. Lust, Cesium carborane as an unconventional non-aqueous electrolyte salt for electrochemical capacitors, Electrochim. Acta. 125 (2014) 482–487. doi:10.1016/j.electacta.2014.01.145.

[38] A. Jänes, H. Kurig, T. Romann, E. Lust, Novel doubly charged cation based electrolytes for non-aqueous supercapacitors, Electrochem. Commun. 12 (2010) 535–539. doi:10.1016/j.elecom.2010.01.037.

[39] H. Kurig, A. Jänes, E. Lust, Substituted phosphonium cation based electrolytes for nonaqueous electrical double-layer capacitors, J. Mater. Res. 25 (2010) 1447–1450. doi:10.1557/JMR.2010.0185.

ACCEPTED MANUSCRIPT

[40] H. Kurig, A. Jänes, E. Lust, Electrochemical Characteristics of Carbide-Derived Carbon|1-Ethyl-3-methylimidazolium Tetrafluoroborate Supercapacitor Cells, J. Electrochem. Soc. 157 (2010) A272–A279. doi:10.1149/1.3274208.

[41] N. Shpigel, M. D. Levi, S. Sigalov, O. Girshevitz, D. Aurbach, L. Daikhin, P. Pikma, M. Marandi, A. Jänes, E. Lust, N. Jäckel, V. Presser, *In situ* hydrodynamic spectroscopy for structure characterization of porous energy storage electrodes, Nat. Mater. 15 (2016) 570–575. doi:10.1038/nmat4577.

[42] S. Sigalov, M.D. Levi, G. Salitra, D. Aurbach, A. Jänes, E. Lust, I.C. Halalay, Selective adsorption of multivalent ions into TiC-derived nanoporous carbon, Carbon 5 (2012) 3957-3960. doi: 10.1016/j.carbon.2012.04.002.

[43] R. Väli, A. Jänes, E. Lust, Vinylene Carbonate as Co-Solvent for Low-Temperature Mixed Electrolyte Based Supercapacitors, J. Electrochem. Soc. 163 (2016) A851–A857. doi:10.1149/2.0541606jes.

[44] A. Jänes, L. Permann, P. Nigu, E. Lust, Influence of solvent nature on the electrochemical characteristics of nanoporous carbon|1 M $(C_2H_5)_3CH_3NBF_4$ electrolyte solution interface, Surf. Sci. 560 (2004) 145–157. doi:10.1016/j.susc.2004.04.026.

[45] A. Jänes, E. Tee, I. Tallo, T. Thomberg, E. Lust, Carbon Dioxide Activated SiC-CDC: Attractive Material for Supercapacitor Electrodes, ECS Trans. 69 (2015) 1–10. doi:10.1149/06924.0001ecst.

[46] T. Tooming, T. Thomberg, H. Kurig, A. Jänes, E. Lust, High power density supercapacitors based on the carbon dioxide activated d-glucose derived carbon

electrodes and 1-ethyl-3-methylimidazolium tetrafluoroborate ionic liquid, J. Power Sources. 280 (2015) 667–677. doi:10.1016/j.jpowsour.2015.01.157.

[47] R. Palm, H. Kurig, K. Tõnurist, A. Jänes, E. Lust, Is the mixture of 1-ethyl-3-methylimidazolium tetrafluoroborate and 1-butyl-3-methylimidazolium tetrafluoroborate applicable as electrolyte in electrical double layer capacitors?, Electrochem. Commun. 22 (2012) 203–206. doi:10.1016/j.elecom.2012.06.029.

[48] T. Tooming, T. Thomberg, L. Siinor, K. Tõnurist, A. Jänes, E. Lust, A Type High Capacitance Supercapacitor Based on Mixed Room Temperature Ionic Liquids Containing Specifically Adsorbed Iodide Anions, J. Electrochem. Soc. 161 (2014) A222–A227. doi:10.1149/2.014403jes.

[49] R. Palm, H. Kurig, K. Tonurist, A. Jaenes, E. Lust, Electrical double layer capacitors based on 1-ethyl-3-methylimidazolium tetrafluoroborate with small addition of acetonitrile, Electrochim. Acta. 85 (2012) 139–144. doi:10.1016/j.electacta.2012.08.030.

[50] A. Jänes, J. Eskusson, T. Thomberg, T. Romann, E. Lust, Ionic liquid-1,2-dimethoxyethane mixture as electrolyte for high power density supercapacitors, J. Energy Chem. 25 (2016) 609–614. doi:10.1016/j.jechem.2016.02.011.

[51] T. Romann, O. Oll, P. Pikma, H. Tamme, E. Lust, Surface chemistry of carbon electrodes in 1-ethyl-3-methylimidazolium tetrafluoroborate ionic liquid – an *in situ* infrared study, Electrochim. Acta. 125 (2014) 183–190. doi:10.1016/j.electacta.2014.01.077.

ACCEPTED MANUSCRIPT

[52] T. Romann, O. Oll, P. Pikma, K. Kirsimäe, E. Lust, 4–10 V capacitors with graphene-based electrodes and ionic liquid electrolyte, J. Power Sources. 280 (2015) 606–611. doi:10.1016/j.jpowsour.2015.01.153.

[53] A. Tõnisoo, J. Kruusma, R. Pärna, A. Kikas, M. Hirsimäki, E. Nõmmiste, E. Lust, In Situ XPS Studies of Electrochemically Negatively Polarized Molybdenum Carbide Derived Carbon Double Layer Capacitor Electrode, J. Electrochem. Soc. 160 (2013) A1084–A1093. doi:10.1149/2.042308jes.

[54] J. Kruusma, A. Tõnisoo, R. Pärna, E. Nõmmiste, E. Lust, In situ XPS studies of electrochemically positively polarized molybdenum carbide derived carbon double layer capacitor electrode, J. Electrochem. Soc. 161 (2014) A1266–A1277. doi:10.1149/2.0641409jes.

[55] J. Kruusma, A. Tõnisoo, R. Pärna, E. Nõmmiste, I. Tallo, T. Romann, E. Lust, Influence of the negative potential of molybdenum carbide derived carbon electrode on the *in situ* synchrotron radiation activated X-ray photoelectron spectra of 1-ethyl-3-methylimidazolium tetrafluoroborate, Electrochim. Acta. 206 (2016) 419–426. doi:10.1016/j.electacta.2015.10.060.

[56] J. Kruusma, A. Tõnisoo, R. Pärna, E. Nõmmiste, M. Vahtrus, L. Siinor, I. Tallo, T. Romann, E. Lust, Influence of Iodide Ions Concentration on the Stability of 1-Ethyl-3-methylimidazolium Tetrafluoroborate| Molybdenum Carbide Derived Carbon Electrode Interface, J. Electrochem. Soc. 164 (2017) A1110–A1119.

[57] E. Tee, I. Tallo, T. Thomberg, A. Janes, E. Lust, Supercapacitors Based on Activated Silicon Carbide-Derived Carbon Materials and Ionic Liquid, J. Electrochem. Soc. 163 (2016) A1317–A1325. doi:10.1149/2.0931607jes.

[58] M. Härmas, T. Thomberg, T. Romann, A. Jänes, E. Lust, Carbon for Energy Storage Derived from Granulated White Sugar by Hydrothermal Carbonization and Subsequent Zinc Chloride Activation, J. Electrochem. Soc. 164 (2017) A1866–A1872. doi:10.1149/2.0681709jes.

[59] K. Tõnurist, I. Vaas, T. Thomberg, A. Jänes, H. Kurig, T. Romann, E. Lust, Application of multistep electrospinning method for preparation of electrical double-layer capacitor half-cells, Electrochim. Acta. 119 (2014) 72–77. doi:10.1016/j.electacta.2013.11.155.

[60] K. Tõnurist, T. Thomberg, A. Jänes, T. Romann, V. Sammelselg, E. Lust, Influence of separator properties on electrochemical performance of electrical double-layer capacitors, J. Electroanal. Chem. 689 (2013) 8–20. doi:10.1016/j.jelechem.2012.11.024.

[61] K. Tõnurist, T. Thomberg, A. Jänes, E. Lust, Specific Performance of Supercapacitors at Lower Temperatures Based on Different Separator Materials, J. Electrochem. Soc. 160 (2013) A449–A457. doi:10.1149/2.044303jes.

[62] H. Kurig, T. Romann, A. Jänes, E. Lust, Electrochemical Characteristics of Titanium Carbide Derived Carbon|1-Ethyl-3-Methylimidazolium Tetrafluoroborate Electrical Double Layer Capacitors, ECS Trans. 25 (2010) 15–23. doi:10.1149/1.3328507.

[63] R. Palm, H. Kurig, T. Romann, U. Joost, R. Kanarbik, R. Väli, I. Tallo, T. Thomberg, A. Jänes, E. Lust, Application of Some Carbon Fabrics as Outstanding Supercapacitor Electrode Materials in Acetonitrile Based Electrolyte, J. Electrochem. Soc. 164 (2017) A453–A460. doi:10.1149/2.0831702jes.

ACCEPTED MANUSCRIPT

[64] J. Jagiello, Stable Numerical Solution of the Adsorption Integral Equation Using Splines, Langmuir. 10 (1994) 2778–2785. doi:10.1021/la00020a045.

[65] S. Brunauer, P.H. Emmett, E. Teller, Adsorption of Gases in Multimolecular Layers, J. Am. Chem. Soc. 60 (1938) 309–319. doi:10.1021/ja01269a023.

[66] D.D. Do, Adsorption Analysis: Equilibria and Kinetics, Imperial College Press, London, 1998.

[67] R. Härmas, R. Palm, M. Härmas, M. Pohl, H. Kurig, I. Tallo, E. Tee, I. Vaas, R. Väli, T. Romann, O. Oll, R. Kanarbik, K. Liivand, J. Eskusson, J. Kruusma, T. Thomberg, A. Jänes, P. Miidla, E. Lust, Detailed Analysis of Carbon Materials for High Power Density Supercapacitors, MethodsX, submitted (2018).

[68] E. Lust, A. Tõnisoo, T. Romann, O. Oll, V. Ivaništšev, R. Kanarbik, J. Kruusma, R. Pärna, A. Kikas, E. Nõmmiste, In Situ XPS and FTIR Studies of Electrochemically Polarized Carbide Derived Carbon and Other Carbon Electrodes in RTILs, Meet. Abstr. MA2015-02 (2015) 430–430.

[69] P.L. Taberna, P. Simon, J.F. Fauvarque, Electrochemical Characteristics and Impedance Spectroscopy Studies of Carbon-Carbon Supercapacitors, J. Electrochem. Soc. 150 (2003) A292–A300. doi:10.1149/1.1543948.

[70] M.E. Orazem, N. Pébère, B. Tribollet, Enhanced Graphical Representation of Electrochemical Impedance Data, J. Electrochem. Soc. 153 (2006) B129–B136. doi:10.1149/1.2168377.

[71] A.V. Neimark, Y. Lin, P.I. Ravikovitch, M. Thommes, Quenched Solid density functional theory and pore size analysis of micro- mesoporous carbons, Carbon, 47 (2009) 1617-1623. 10.1016/j.carbon.2009.01.050.

[72] P. Kleszyk, P. Ratajczak, P. Skowron, J. Jagiello, Q. Abbas, E. Frąckowiak, F. Béguin, Carbons with narrow pore size distribution prepared by simultaneous carbonization and self-activation of tobacco stems and their application to supercapacitors, Carbon 81 (2015) 148–157. doi:10.1016/j.carbon.2014.09.043.

[73] M.Thommes, C. Morlay, R. Ahmad, J.P. Joly, Assessing surface chemistry and pore structure of active carbons by a combination of physisorption (H_2O, Ar, N_2, CO_2), XPS and TPD-MS, Adsorption 17 (2011) 653-661. doi: 10.1007/s10450-011-9360-4.

[74] H. Kurig, Examples of application of Neutron Scattering: Carbons. Summer school "Neutorn Scattering Applications to Hydrogen Storage Materials", Berlin 17-26.08.2015.

[75] E. Härk, N. Kardjilov, A. Hilger, A. Petzold, S. Risse, I. Vaas, G. Goerigk, C. Jafta, M. Ballauff, E. Lust, The Nanoporous RP-20 Carbon Electrode as a Model for Energy Storage and Conversion Systems – Studied with µCT, SAXS and SANS Techniques, ECS Trans. 77 (2017) 1133–1144. doi:10.1149/07711.1133ecst.

[76] M.A. Pimenta, G. Dresselhaus, M.S. Dresselhaus, L.G. Cançado, A. Jorio, R. Saito, Studying disorder in graphite-based systems by Raman spectroscopy, Phys. Chem. Chem. Phys. 9 (2007) 1276–1290. doi:10.1039/B613962K.

[77] A.C. Ferrari, J. Robertson, Interpretation of Raman spectra of disordered and amorphous carbon, Phys. Rev. B. 61 (2000) 14095–14107. doi:10.1103/PhysRevB.61.14095.

[78] Y. Korenblit, M. Rose, E. Kockrick, L. Borchardt, A. Kvit, S. Kaskel, G. Yushin, High-Rate Electrochemical Capacitors Based on Ordered Mesoporous Silicon Carbide-Derived Carbon, ACS Nano. 4 (2010) 1337–1344. doi:10.1021/nn901825y.

[79] S. Urbonaite, Synthesis and characterisation of Carbide derived Carbons, Department of Physical, Inorganic and Structural Chemistry, Stockholm University, 2008.

[80] C. Hu, S. Sedghi, A. Silvestre-Albero, G.G. Andersson, A. Sharma, P. Pendleton, F. Rodríguez-Reinoso, K. Kaneko, M.J. Biggs, Raman spectroscopy study of the transformation of the carbonaceous skeleton of a polymer-based nanoporous carbon along the thermal annealing pathway, Carbon. 85 (2015) 147–158. doi:10.1016/j.carbon.2014.12.098.

[81] F. Tuinstra, J.L. Koenig, Raman Spectrum of Graphite, J. Chem. Phys. 53 (1970) 1126–1130. doi:10.1063/1.1674108.

[82] D.S. Knight, W.B. White, Characterization of diamond films by Raman spectroscopy, J. Mater. Res. 4 (1989) 385–393. doi:10.1557/JMR.1989.0385.

[83] A. Sadezky, H. Muckenhuber, H. Grothe, R. Niessner, U. Pöschl, Raman microspectroscopy of soot and related carbonaceous materials: Spectral analysis and structural information, Carbon. 43 (2005) 1731–1742. doi:10.1016/j.carbon.2005.02.018.

[84] G.A. Zickler, B. Smarsly, N. Gierlinger, H. Peterlik, O. Paris, A reconsideration of the relationship between the crystallite size La of carbons determined by X-ray diffraction and Raman spectroscopy, Carbon. 44 (2006) 3239–3246. doi:10.1016/j.carbon.2006.06.029.

[85] P. Mallet-Ladeira, P. Puech, C. Toulouse, M. Cazayous, N. Ratel-Ramond, P. Weisbecker, G.L. Vignoles, M. Monthioux, A Raman study to obtain crystallite size

of carbon materials: A better alternative to the Tuinstra–Koenig law, Carbon. 80 (2014) 629–639. doi:10.1016/j.carbon.2014.09.006.

[86] J. Ribeiro-Soares, M.E. Oliveros, C. Garin, M.V. David, L.G.P. Martins, C.A. Almeida, E.H. Martins-Ferreira, K. Takai, T. Enoki, R. Magalhães-Paniago, A. Malachias, A. Jorio, B.S. Archanjo, C.A. Achete, L.G. Cançado, Structural analysis of polycrystalline graphene systems by Raman spectroscopy, Carbon. 95 (2015) 646–652. doi:10.1016/j.carbon.2015.08.020.

[87] L.G. Cançado, K. Takai, T. Enoki, M. Endo, Y.A. Kim, H. Mizusaki, A. Jorio, L.N. Coelho, R. Magalhães-Paniago, M.A. Pimenta, General equation for the determination of the crystallite size La of nanographite by Raman spectroscopy, Appl. Phys. Lett. 88 (2006) 163106. doi:10.1063/1.2196057.

[88] N. Shimodaira, A. Masui, Raman spectroscopic investigations of activated carbon materials, J. Appl. Phys. 92 (2002) 902–909. doi:10.1063/1.1487434.

[89] Y. Kawashima, G. Katagiri, Fundamentals, overtones, and combinations in the Raman spectrum of graphite, Phys. Rev. B. 52 (1995) 10053–10059. doi:10.1103/PhysRevB.52.10053.

[90] J.-M. Vallerot, X. Bourrat, A. Mouchon, G. Chollon, Quantitative structural and textural assessment of laminar pyrocarbons through Raman spectroscopy, electron diffraction and few other techniques, Carbon. 44 (2006) 1833–1844. doi:10.1016/j.carbon.2005.12.029.

[91] A.C. Forse, C. Merlet, P.K. Allan, E.K. Humphreys, J.M. Griffin, M. Aslan, M. Zeiger, V. Presser, Y. Gogotsi, C.P. Grey, New Insights into the Structure of

Nanoporous Carbons from NMR, Raman, and Pair Distribution Function Analysis, Chem. Mater. 27 (2015) 6848–6857. doi:10.1021/acs.chemmater.5b03216.

[92] L.G. Cançado, K. Takai, T. Enoki, M. Endo, Y.A. Kim, H. Mizusaki, N.L. Speziali, A. Jorio, M.A. Pimenta, Measuring the degree of stacking order in graphite by Raman spectroscopy, Carbon. 46 (2008) 272–275. doi:10.1016/j.carbon.2007.11.015.

[93] Y.-J. Lee, The second order Raman spectroscopy in carbon crystallinity, J. Nucl. Mater. 325 (2004) 174–179. doi:10.1016/j.jnucmat.2003.12.005.

[94] C. Largeot, C. Portet, J. Chmiola, P.-L. Taberna, Y. Gogotsi, P. Simon, Relation between the Ion Size and Pore Size for an Electric Double-Layer Capacitor, J. Am. Chem. Soc. 130 (2008) 2730–2731. doi:10.1021/ja7106178.

[95] B. Lobato, L. Suárez, L. Guardia, T.A. Centeno, Capacitance and surface of carbons in supercapacitors, Carbon. 122 (2017) 434–445. doi:10.1016/j.carbon.2017.06.083.

[96] T. A. Centeno, O. Sereda, F. Stoeckli, Capacitance in carbon pores of 0.7 to 15 nm: a regular pattern, Phys. Chem. Chem. Phys. 13 (2011) 12403–12406. doi:10.1039/C1CP20748B.

[97] Q. Xie, G. Chen, R Bao, Y. Zhang, S. Wu, Polystyrene foam derived nitrogen-enriched porous carbon/graphene composites with high volumetric capacitances for aqueous supercapacitors, Micropor. Mesopor. Mater. 239 (2017) 130–137. 10.1016/j.micromeso.2016.10.007.

[98] R.Yan, T.Heil, V.Presser, R. Walczak, M. Antonietti, M. Oschatz, Ordered Mesoporous Carbons with High Micropore Content and Tunable Structure Prepared

by Combined Hard and Salt Templating as Electrode Materials in Electric Double-Layer Capacitors, Adv. Sustainable Syst. 2 (2018) 1700128 (1–12). 10.1002/adsu.201700128.

[99] T.A. Centeno, F. Stoeckli, The assessment of surface areas in porous carbons by two model-independent techniques, the DR equation and DFT, Carbon. 48 (2010) 2478–2486. doi:10.1016/j.carbon.2010.03.020.

[100] J.A. Fernández, M. Arulepp, J. Leis, F. Stoeckli, T.A. Centeno, EDLC performance of carbide-derived carbons in aprotic and acidic electrolytes, Electrochim. Acta. 53 (2008) 7111–7116. doi:10.1016/j.electacta.2008.05.028.

[101] T.A. Centeno, J.A. Fernandez, F. Stoeckli, Correlation between heats of immersion and limiting capacitances in porous carbons, Carbon. 46 (2008) 1025–1030. doi:10.1016/j.carbon.2008.03.005.

[102] G. Lota, T.A. Centeno, E. Frackowiak, F. Stoeckli, Improvement of the structural and chemical properties of a commercial activated carbon for its application in electrochemical capacitors, Electrochim. Acta. 53 (2008) 2210–2216. doi:10.1016/j.electacta.2007.09.028.

[103] T.A. Centeno, M. Hahn, J.A. Fernández, R. Kötz, F. Stoeckli, Correlation between capacitances of porous carbons in acidic and aprotic EDLC electrolytes, Electrochem. Commun. 9 (2007) 1242–1246. doi:10.1016/j.elecom.2007.01.031.

[104] E. Raymundo-Piñero, F. Leroux, F. Béguin, A High-Performance Carbon for Supercapacitors Obtained by Carbonization of a Seaweed Biopolymer, Adv. Mater. 18 (2006) 1877–1882. doi:10.1002/adma.200501905.

[105] M. Lazzari, F. Soavi, M. Mastragostino, Mesoporous Carbon Design for Ionic Liquid-Based, Double-Layer Supercapacitors, Fuel Cells. 10 (2010) 840–847. doi:10.1002/fuce.200900198.

[106] R. Palm, I. Tallo, T. Romann, H. Kurig, Methane adsorption on specially designed TiC and Mo2C derived carbons with different pore size and surface morphology, Microporous Mesoporous Mater. 218 (2015) 167–173. doi:10.1016/j.micromeso.2015.07.016.

ACCEPTED MANUSCRIPT

Tables

Table 1. Parameters of fitting functions for C_s vs. S_{DFT} and C_s vs. V_{DFT} dependences presented as red lines in Figs. 12a–12c; 15b–15d; 16b and 16c, respectively. Statistical data are included in Table, more detailed analysis is given in Härmas et al. [67].

Table 2. Specific surface area and pore volumes of carbon powders calculated form N_2 adsorption isotherms using 2D-NLDFT-HS model. Specific surface areas and pore volumes were calculated including all pore sizes (noted here as $S_{DFT,tot}$ and $V_{DFT,tot}$) and for pores with sizes $w > 0.7$ nm (noted here as S_{DFT} and V_{DFT}). More information is given in Härmas et al. [67].

ACCEPTED MANUSCRIPT

Figures

Fig. 1. Nitrogen adsorption data for TiC-CDC, Mo_2C-CDC and SiC-CDC 1100 (activated with H_2O and chemically reduced with H_2) and D-glucose derived CO_2 activated carbon (GDC-CO_2) synthesized at different chlorination temperatures (noted in Figure): N_2 isotherms and fits (given in Figure) to the experimental isotherms calculated applying the 2D-NLDFT-HS model (SAIEUS, Micromeritics. More detailed analysis of data is given in Härmas et al. [67].

Fig. 2. Experimental N_2, CO_2 and Ar adsorption isotherms with fittings (a) and cumulative pore volume vs. pore width dependences (b) for SiC-CDC 1100 (activated with H_2O and chemically reduced with H_2) calculated by 2D-NLDFT-HS model.

Fig. 3. Pore size distribution (dS_{DFT}/dw) vs. pore width (w) plots for SiC-CDC 1100 (activated with H_2O and chemically reduced with H_2) (a) and SiC-CDC 1100 (activated with H_2O) (b) obtained by 2D-NLDFT-HS model.

Fig. 4. Experimental N_2 adsorption isotherms for SiC-CDC 1100 (activated with H_2O and chemically reduced with H_2) and fittings obtained by various NLDFT models (noted in Figure) (a), and pore size distribution (dS_{DFT}/dw) vs. pore width (w) plots (b) calculated

with different NLDFT models implemented in SAIEUS (Micromeritics) (noted in Figure).

Fig. 5. XRD data for WC-CDC materials (a) (chlorination temperatures noted in Figure); crystallite size (L_a) values (b) calculated with Scherrer equation for different carbide derived carbons (noted in Figure); high-resolution TEM data for WC-CDC 800 (c) and WC-CDC 1000 (d) with selected area electron diffraction (SAED) and electron energy loss spectroscopy (EELS) data (the insets of (c) and (d)). Additional information is given in Härmas et al. [67].

Fig. 6. Characteristic XRD patterns for (a) Mo_2C-CDC synthesized at different temperatures (noted in Figure), for carbons derived from D-glucose and white sugar (b) (noted in Figure); for SiC-CDC 1100 at different after-treatment conditions (c) (noted in Figure, A1 – activation burn-off 19%, A2 – activation burn-off 29%, and A3 – activation burn-off 68%); sol-gel method TiC-CDC chlorinated at T = 1100 ºC with and without added carbon nanotubes (d) (in w%, noted in Figure).

Fig. 7. TEM images for Mo_2C-CDC 800 (I), SiC-CDC 1100 (II), and SiC-CDC 1100 A2 (III); SEM images for GDC-CO_2-0h (IV), GDC-CO_2-12h (V), and sol-gel method TiC-CDC (without nanotubes) (VI); HRTEM images for GDC-0h (VII), and GDC-CO_2-12h (VIII); SEM image for sol-gel method prepared TiC/2%CNT-CDC (a). Operando SR XPS data for Mo_2C-CDC 800 (b) (details are given in Figure).

Fig. 8. Raman spectra for Mo_2C-CDC synthesized at different chlorination temperatures (a) (noted in Figure), for D-glucose derived carbon powders with different activation times (b) (noted in Figure) at 900 °C, and for SiC-CDC with different after treatments (c) (noted in Figure, A1 – activation burn-off 19%, A2 – activation burn-off 29%, and A3 – activation burn-off 68%); and for Sol-gel method TiC-CDC chlorinated at 1100 ºC with and without added carbon nanotubes (d) (in w%, noted in Figure).

Fig. 9. Parameter S'_D/S'_G (as proposed by Ribeiro-Soares et al. [80]) vs. synthesis temperature (T_{syn}) for the carbide-derived carbons (a) and full-width half maximum of the D-peak ($FWHM_D$) vs. T_{syn} dependences (b).

Fig. 10. The dependences of integral capacitance (C_{CV}, calculated from cyclic voltammetry data) on cell potential (ΔE) at different potential scan rates (a) (noted in Figure) for GDC-CO_2 12 h, and capacitance retention vs. potential sweep rate (ν) curves (calculated from CV data) for different GDC-CO_2 electrodes (b) (noted in Figure) in 1 M Et_3MeNBF_4 + AN electrolyte.

Fig. 11. Series capacitance (C_s) and parallel capacitance (C_p) (noted in Figure) vs. *ac* frequency plots for the EDLCs based on the different carbon electrodes (noted in Figure and Table 2) in 1 M Et_3MeNBF_4 solution in AN (a) and in $EtMeImBF_4$ ionic liquid (b) at cell potential ΔE = 3.0 V.

Fig. 12. Dependences of series capacitance (at 1 mHz) on specific surface area, S_{DFT}, (a,c) and on total pore volume, V_{DFT}, (b) calculated by 2D-NLDFT-HS model for pores larger than 0.7 nm for various electrodes (noted in Figure and Tables 1 and 2) in 1 M Et_3MeNBF_4 solution in AN (a, b) and in $EtMeImBF_4$ ionic liquid (c) at ΔE = 3,0 V. The error corridor is given in Figure. The confidence band limits at 95% from an area within the fitted red line is with a confidence of 95% are given. The prediction band limit at 95% form an area within which the next experimental point will be with a confidence of 95%. The fits and the corresponding fit confidence and prediction band limits were calculated using the OriginPro 2015 software.

Fig. 13. Imaginary part of capacitance vs. *ac* frequency plots for the EDLCs based on the different carbon materials (noted in Figure) in 1 M Et_3MeNBF_4 solution in AN (a), and in $EtMeImBF_4$ ionic liquid (b) at cell potential ΔE = 3.0 V. More detailed information is given in Härmas et al. [67].

Fig. 14. Dependences of relaxation time constants (τ_{char}) on specific surface area (S_{DFT}) (a,c) and total pore volume (V_{DFT}) (b), calculated with 2D-NLDFT-HS model for pores larger than 0.7 nm, for various electrodes (noted in Figure and Table 2) in 1 M Et_3MeNBF_4 solution in AN (a,b,d) and in $EtMeImBF_4$ ionic liquid (c). The values of τ_{char} are obtained from the intersection points of the dependences of normalized active power ($|P|/|S|$) and reactive power ($|Q|/|S|$) on *ac* frequency calculated from EIS data (Eqs. 5-10). More detailed information is given in Härmas et al. [67].

Fig. 15. Experimental gravimetric Ragone plots for different carbon materials and electrolytes based two-electrode cells (a) (noted in Figure). Dependences of gravimetric power densities at 3.6 s ($P_{3.6s}$) (b,c) and 0.36 s ($P_{0.36s}$) (d) discharge times on specific surface area (b) and total pore volume (c,d), calculated with 2D-NLDFT-HS model for pores larger than 0.7 nm for different electrodes (noted in Figure) in 1 M Et_3MeNBF_4 + AN. The confidence band limits at 95% from an area within the fitted red line is with a confidence of 95% are given. The prediction band limit at 95% form an area within which the next experimental point will be with a confidence of 95%. The fits and the corresponding fit confidence and prediction band limits were calculated using the OriginPro 2015 software. The 3D fit of $P_{0.36s}$ (e) and $P_{3.6s}$ (f) calculated from data in Figs. 15e and 15f using the mathematical method described Härmas et al. [67].

Fig. 16. Experimental volumetric Ragone plots for the two-electrode cells based on different carbon materials and electrolytes (a) (noted in Figure). Volumetric power densities at 0.36 s discharge time ($P_{0.36s}$) vs. S_{DFT} (b) and vs. V_{DFT} (c) for various electrodes (noted in Figure and Table 2) in 1 M Et_3MeNBF_4 solution in AN. The confidence band limits at 95% from an area within the fitted red line is with a confidence of 95% are given. The prediction band limit at 95% form an area within which the next experimental point will be with a confidence of 95%. The fits and the corresponding fit confidence and prediction band limits were calculated using the OriginPro 2015 software. The 3D fit of $P_{0.36s}$ (d) for EDLCs under study.

Table 1. Parameters of fitting functions for C_s vs. S_{DFT} and C_s vs. V_{DFT} dependences presented as red lines in Figs. 12a–12c; 15b–15d; 16b and 16c, respectively. Statistical data are included in Table, more detailed analysis is given in Härmas et al. [67].

1 M Et_3MeNBF_4 in AN electrolyte Fitting function: $y = a(1 - \exp(-bx))$						
y	x	R^2	a	a error	b	b error
C_s (F g^{-1})	S_{DFT} (m^2 g^{-1})	0.8165	128.8	3.9	0.00322	0.00037
C_s (F g^{-1})	V_{DFT} (cm^3 g^{-1})	0.7241	126.4	4.0	5.57	0.69
$P_{3.6s}$ (kW kg^{-1})	S_{DFT} (m^2 g^{-1})	0.6071	35.93	9.03	8.93E-4	3.56E-4
$P_{3.6s}$ (kW kg^{-1})	V_{DFT} (cm^3 g^{-1})	0.6556	28.56	2.08	1.94	0.30
$P_{0.36s}$ (kW kg^{-1})	V_{DFT} (cm^3 g^{-1})	0.8228	324.5	79.1	0.270	0.087
$P_{0.36s}$ (kW dm^{-3})	S_{DFT} (m^2 g^{-1})	0.5645	45.15	3.34	2.49E-3	6.15E-4
$P_{0.36s}$ (kW dm^{-3})	V_{DFT} (cm^3 g^{-1})	0.5512	43.84	1.41	4.68	0.95
$EtMeImBF_4$ electrolyte Fitting function: $y = a(1 - \exp(-bx))$						
y	x	R^2	a	a error	b	b error
C_s (F g^{-1})	S_{DFT} (m^2 g^{-1})	0.7653	151.4	8.9	3.59E-3	7.3E-4

C_s is the series capacitance of a two-electrode system, S_{DFT} and V_{DFT} are the specific surface area and pore volume of carbon powders calculated with 2D-NLDFT-HS model for pores with sizes $w > 0.7$ nm. $P_{3.6s}$ and $P_{0.36s}$ are the power densities (gravimetric or volumetric, distinguishable based on unit) at discharge times 3.6 s and 0.36 s, respectively.

ACCEPTED MANUSCRIPT

ACCEPTED MANUSCRIPT

Table 2. Specific surface areas and pore volumes of carbon powders (calculated form N_2 adsorption isotherms using the 2D-NLDFT-HS model). Specific surface areas and pore volumes were calculated including all pore sizes (noted here as $S_{DFT,tot}$ and $V_{DFT,tot}$) and for pores with sizes $w > 0.7$ nm (noted as S_{DFT} and V_{DFT}). More information is given in Härmas et al. [67].

Carbon material	$S_{DFT,tot}$ (m^2 g^{-1})	S_{DFT} (m^2 g^{-1})	$V_{DFT,tot}$ (cm^3 g^{-1})	V_{DFT} (cm^3 g^{-1})
GDC:KOH:$ZnCl_2$ (1:4:0)	2000	1190	0.93	0.70
GDC:KOH:$ZnCl_2$ (1:0:4)	1740	1180	0.92	0.76
GDC:KOH:$ZnCl_2$ (1:3:1)	1810	600	0.72	0.36
GDC:KOH:$ZnCl_2$ (1:2:2)	1120	220	0.36	0.10
GDC:KOH:$ZnCl_2$ (1:1:3)	1380	340	0.47	0.18
GDC:KOH:$ZnCl_2$ (1:0:0)	840	90	0.25	0.04
GDC–CO_2 4h	1270	210	0.44	0.14
GDC–CO_2 6h	1440	340	0.48	0.17
GDC-CO_2 8h	1510	400	0.55	0.24
GDC CO_2 10h	1810	680	0.67	0.35
GDC CO_2 12h	1530	470	0.53	0.24
Mo_2C-CDC 800	1740	1360	1.60	1.50
WC-CDC 1100	1190	820	0.76	0.66
WC-CDC 1000	800	800	0.58	0.58
WC-CDC 800	1060	680	0.58	0.47
TiC-CDC 1100	1290	820	0.88	0.74
TiC-CDC 900	1770	740	0.74	0.46
TiC-CDC 700	1720	500	0.61	0.26
TiC-CDC 1100 HCl	690	530	0.86	0.82
TiC-CDC 900 HCl	1050	620	0.63	0.51
TiC-CDC 700 HCl	1040	510	0.49	0.34
Ta_4HfC_5-CDC 800	1830	880	0.79	0.52
Ta_4HfC_5-CDC 900	1740	930	0.80	0.57
Ta_4HfC_5-CDC 1000	1760	1040	0.89	0.68
Ta_4HfC_5-CDC 1100	1670	1050	0.92	0.75
$WTiC_2$-CDC 800	1710	730	0.70	0.42
$WTiC_2$-CDC 900	1800	880	0.79	0.54
$WTiC_2$-CDC 1000	1670	940	0.80	0.59
SiC-CDC 1000 A1	1610	680	0.64	0.37
SiC-CDC 1000 A2	1780	990	0.85	0.63
SiC-CDC 1000 A3	1840	1200	1.06	0.88
SiC-CDC 1100 A1	1660	740	0.69	0.43
SiC-CDC 1100 A2	1800	970	0.84	0.61
SiC-CDC 1100 A3	1780	1240	1.19	1.04
TiC-CDC 950	2090	1600	3.80	3.67
TiC/1%CNT-CDC 950	1820	1330	3.09	2.97
TiC/2%CNT-CDC 950	1490	1220	2.68	2.63

Busofit T-040−1	1370	460	0.56	0.30
Busofit T-040	1440	550	0.59	0.34
Busofit L-0.3−135	800	90	0.25	0.05

GDC:KOH:$ZnCl_2$ (x:y:z) – hydrothermally carbonized glucose activated with KOH and/or $ZnCl_2$, where x denotes HTC carbon, y KOH and z $ZnCl_2$ mass ratio; GDC CO_2- glucose derived carbon activated with CO_2 at 800 °C for 4, 6, 8 and 12 hours. Carbide-derived carbons are noted as X-CDC Y, where X denotes the carbide and Y denotes the chlorination temperature in Celsius degrees. For some materials, HCl was used instead of Cl_2 (noted as X-CDC Y HCl). SiC-CDC 1000An (A - activation temperature and durability n = 1, 2 or 3) – after synthesis at 1000 ºC, CO_2 activation at 900, 950 and 950 °C for 6 h, 3 h and 8 h for A1, A2 and A3, respectively, has been applied. Busofit is a carbon fabric from SvetlogorskKhimvolokno, Belarus, data are given in [63].

ACCEPTED MANUSCRIPT

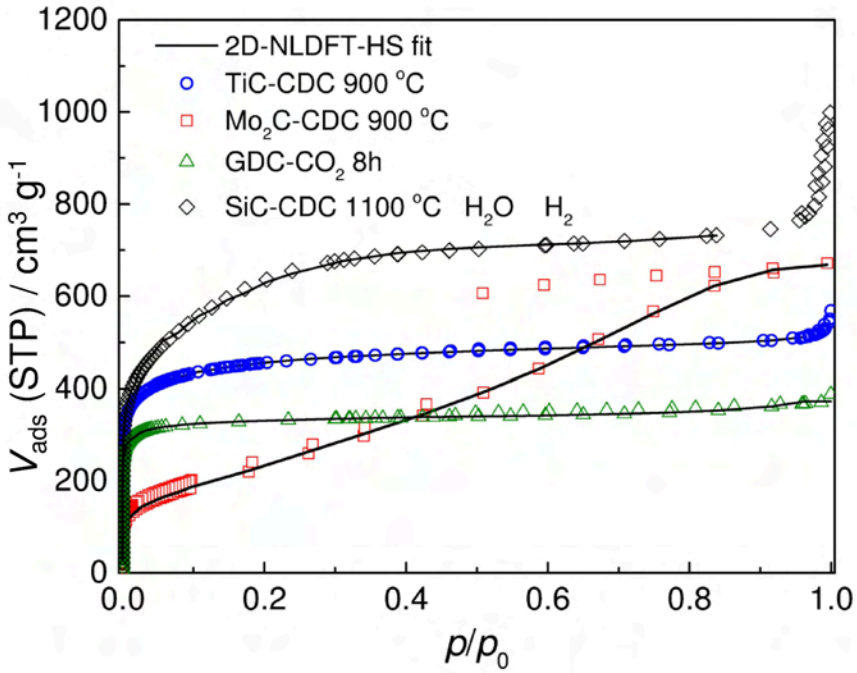
2D-NLDFT-HS fit
TiC-CDC 900 °C
Mo2C-CDC 900 °C
GDC-CO2 8h
SiC-CDC 1100 °C H2O H2
Vads (STP) / cm3 g-1
p/p0
0
200
400
600
800
1000
1200
0.0
0.2
0.4
0.6
0.8
1.0

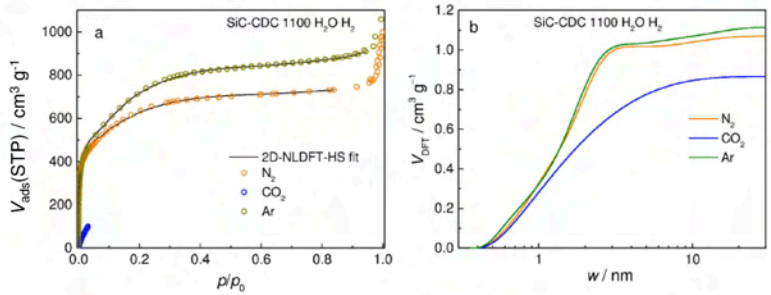
a
SiC-CDC 1100 H2O H2
2D-NLDFT-HS fit
N2
CO2
Ar
Vads(STP) / cm3 g-1
p/p0
b
SiC-CDC 1100 H2O H2
N2
CO2
Ar
VDFT / cm3 g-1
w / nm

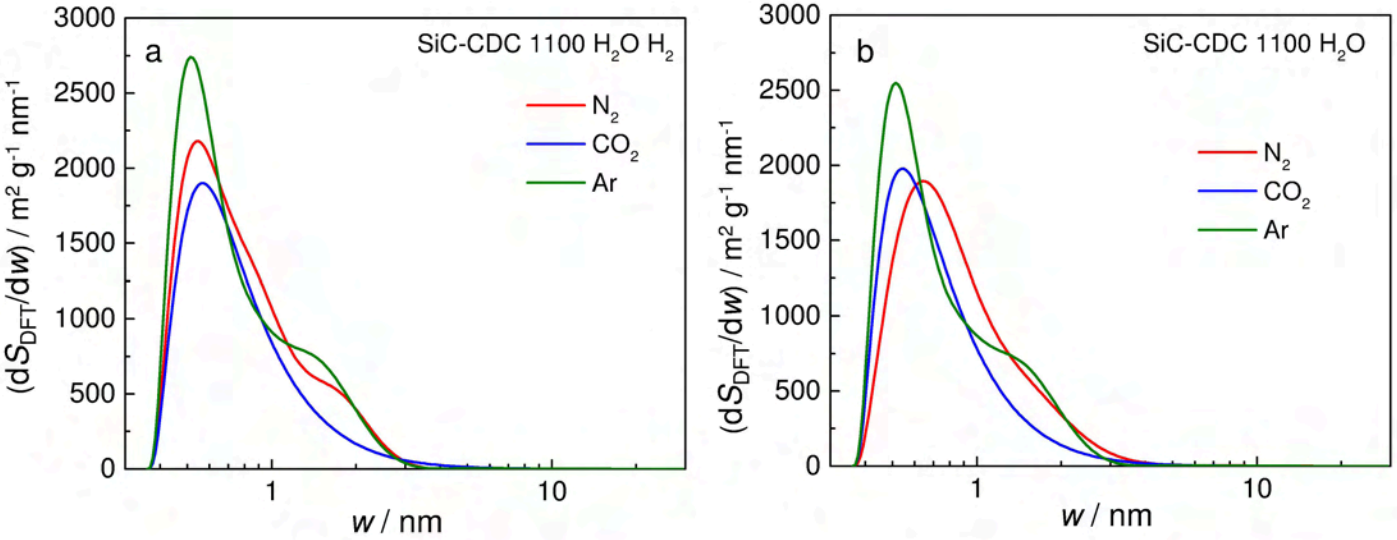
a
SiC-CDC 1100 H2O H2
N2
CO2
Ar
(dSDFT/dw) / m2 g-1 nm-1
w / nm
b
SiC-CDC 1100 H2O
N2
CO2
Ar
(dSDFT/dw) / m2 g-1 nm-1
w / nm

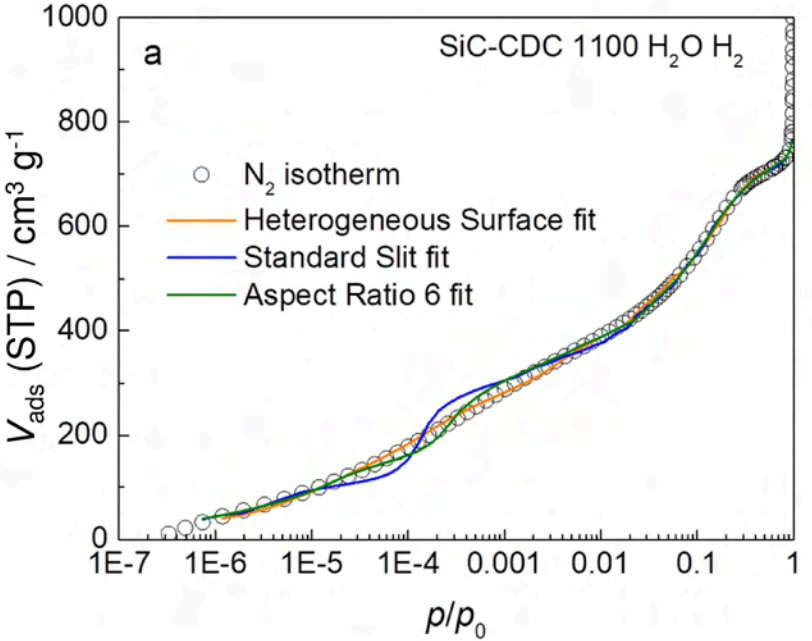
a
SiC-CDC 1100 H2O H2
N2 isotherm
Heterogeneous Surface fit
Standard Slit fit
Aspect Ratio 6 fit
Vads (STP) / cm3 g-1
p/p0
1000
800
600
400
200
0
1E-7
1E-6
1E-5
1E-4
0.001
0.01
0.1
1

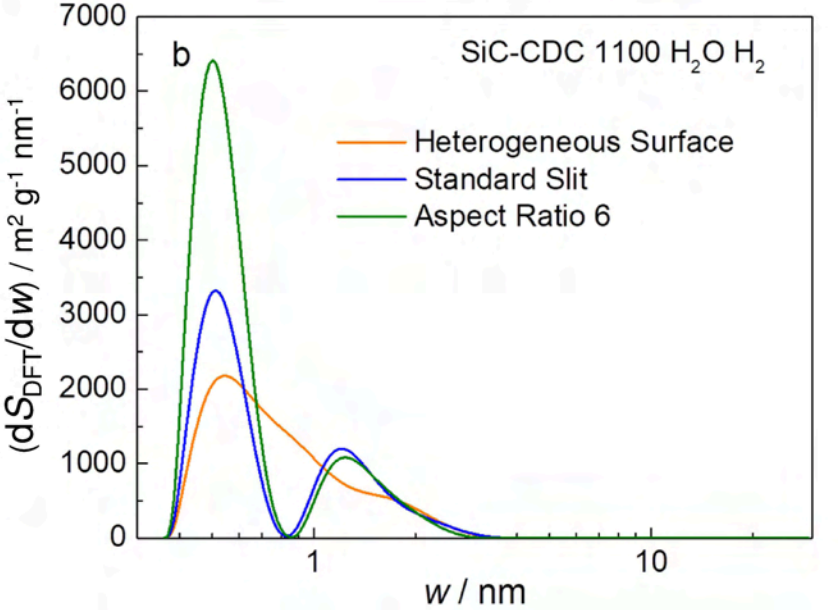
b
SiC-CDC 1100 H2O H2
Heterogeneous Surface
Standard Slit
Aspect Ratio 6
(dSDFT/dw) / m2 g-1 nm-1
w / nm
7000
6000
5000
4000
3000
2000
1000
0
1
10

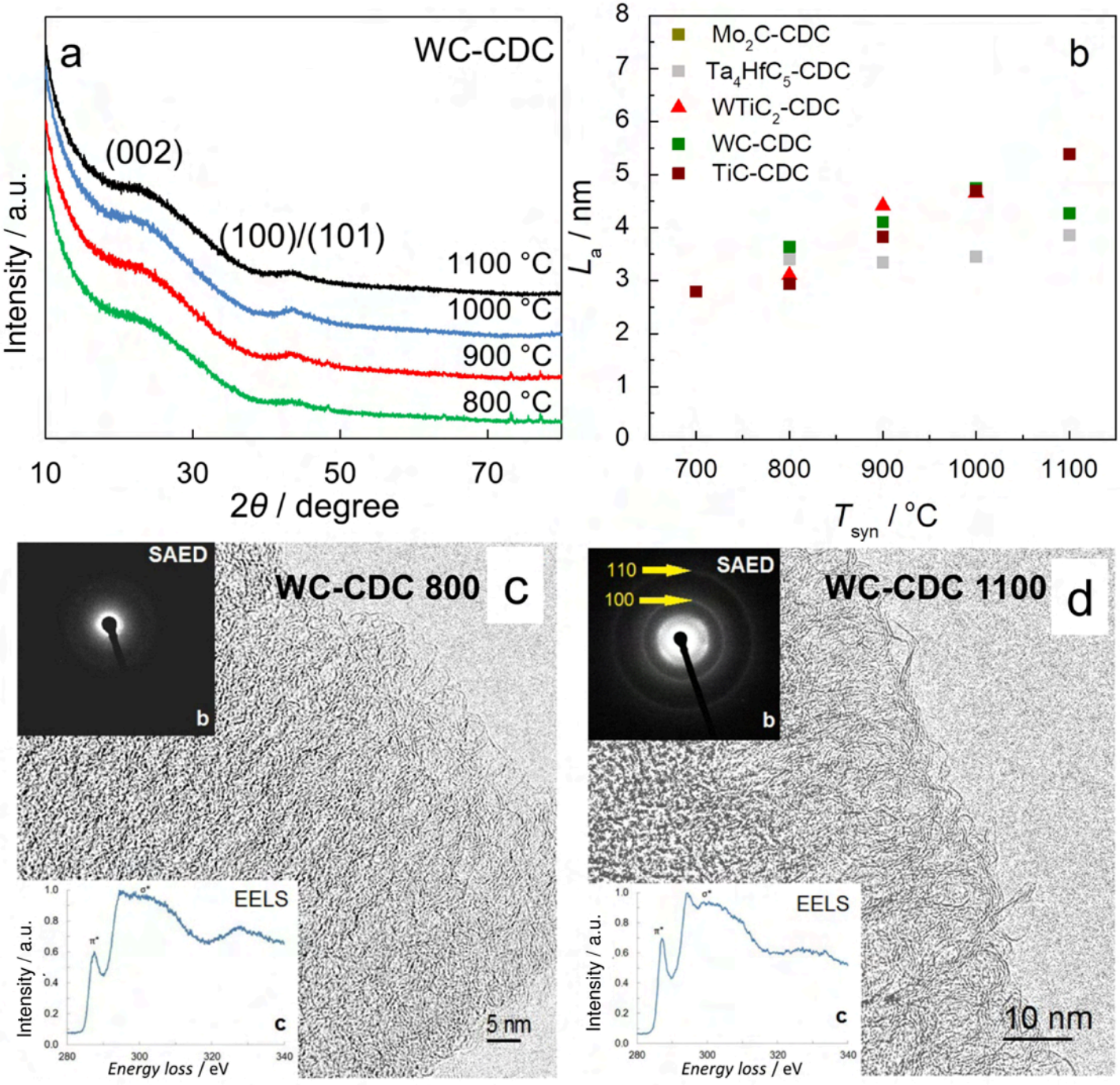
a
WC-CDC
(002)
(100)/(101)
1100 °C
1000 °C
900 °C
800 °C
Intensity / a.u.
10
30
50
70
2θ / degree
b
Mo2C-CDC
Ta4HfC5-CDC
WTiC2-CDC
WC-CDC
TiC-CDC
La / nm
0
1
2
3
4
5
6
7
8
700
800
900
1000
1100
Tsyn / °C
SAED
b
WC-CDC 800
c
EELS
Intensity / a.u.
Energy loss / eV
c
5 nm
110
100
SAED
b
WC-CDC 1100
d
EELS
Intensity / a.u.
Energy loss / eV
c
10 nm

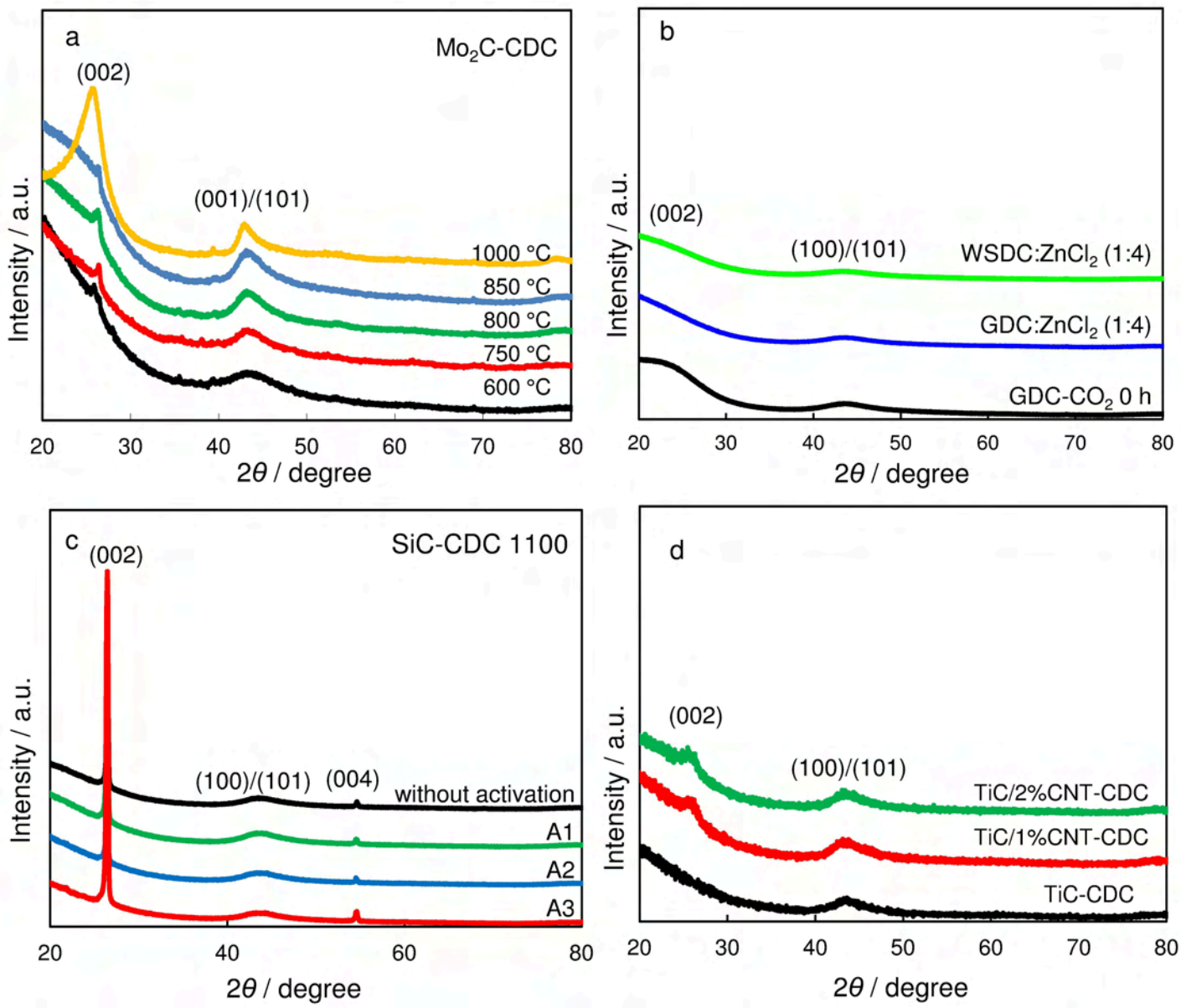
a
Mo2C-CDC
(002)
(001)/(101)
1000 °C
850 °C
800 °C
750 °C
600 °C
Intensity / a.u.
2θ / degree
b
(002)
(100)/(101)
WSDC:ZnCl2 (1:4)
GDC:ZnCl2 (1:4)
GDC-CO2 0 h
Intensity / a.u.
2θ / degree
c
SiC-CDC 1100
(002)
(100)/(101)
(004)
without activation
A1
A2
A3
Intensity / a.u.
2θ / degree
d
(002)
(100)/(101)
TiC/2%CNT-CDC
TiC/1%CNT-CDC
TiC-CDC
Intensity / a.u.
2θ / degree

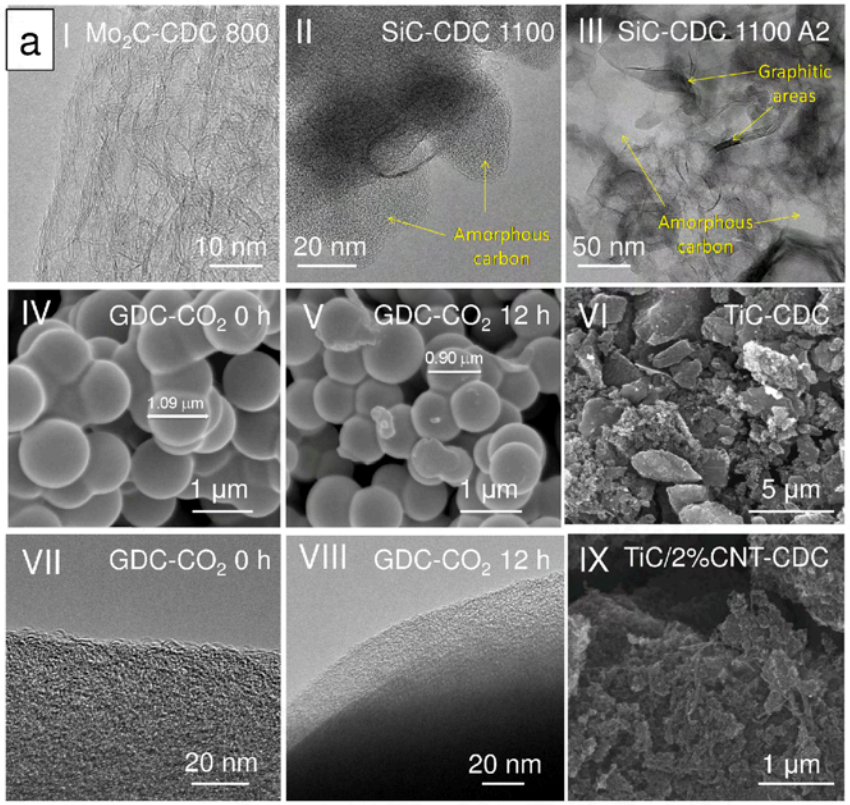
a
I Mo2C-CDC 800
10 nm
II SiC-CDC 1100
20 nm
Amorphous carbon
III SiC-CDC 1100 A2
Graphitic areas
Amorphous carbon
50 nm
IV GDC-CO2 0 h
1.09 µm
1 µm
V GDC-CO2 12 h
0.90 µm
1 µm
VI TiC-CDC
5 µm
VII GDC-CO2 0 h
20 nm
VIII GDC-CO2 12 h
20 nm
IX TiC/2%CNT-CDC
1 µm

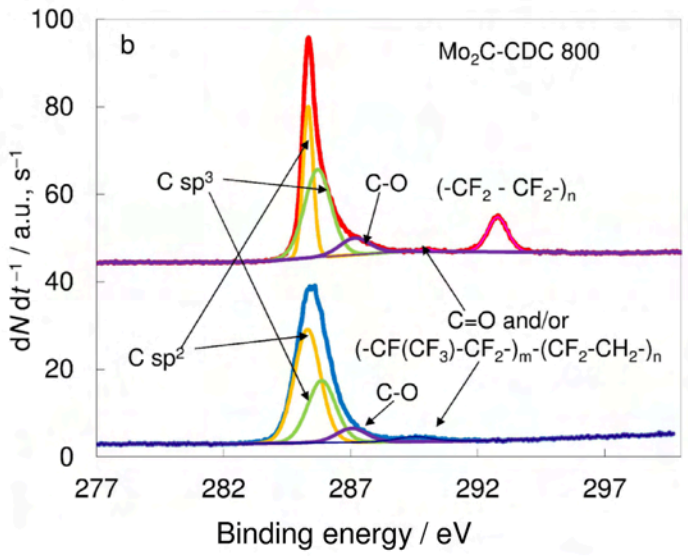
b
Mo2C-CDC 800
C sp3
C-O
(-CF2 - CF2-)n
C=O and/or
(-CF(CF3)-CF2-)m-(CF2-CH2-)n
C sp2
C-O
dN dt-1 / a.u., s-1
Binding energy / eV
100
80
60
40
20
0
277
282
287
292
297

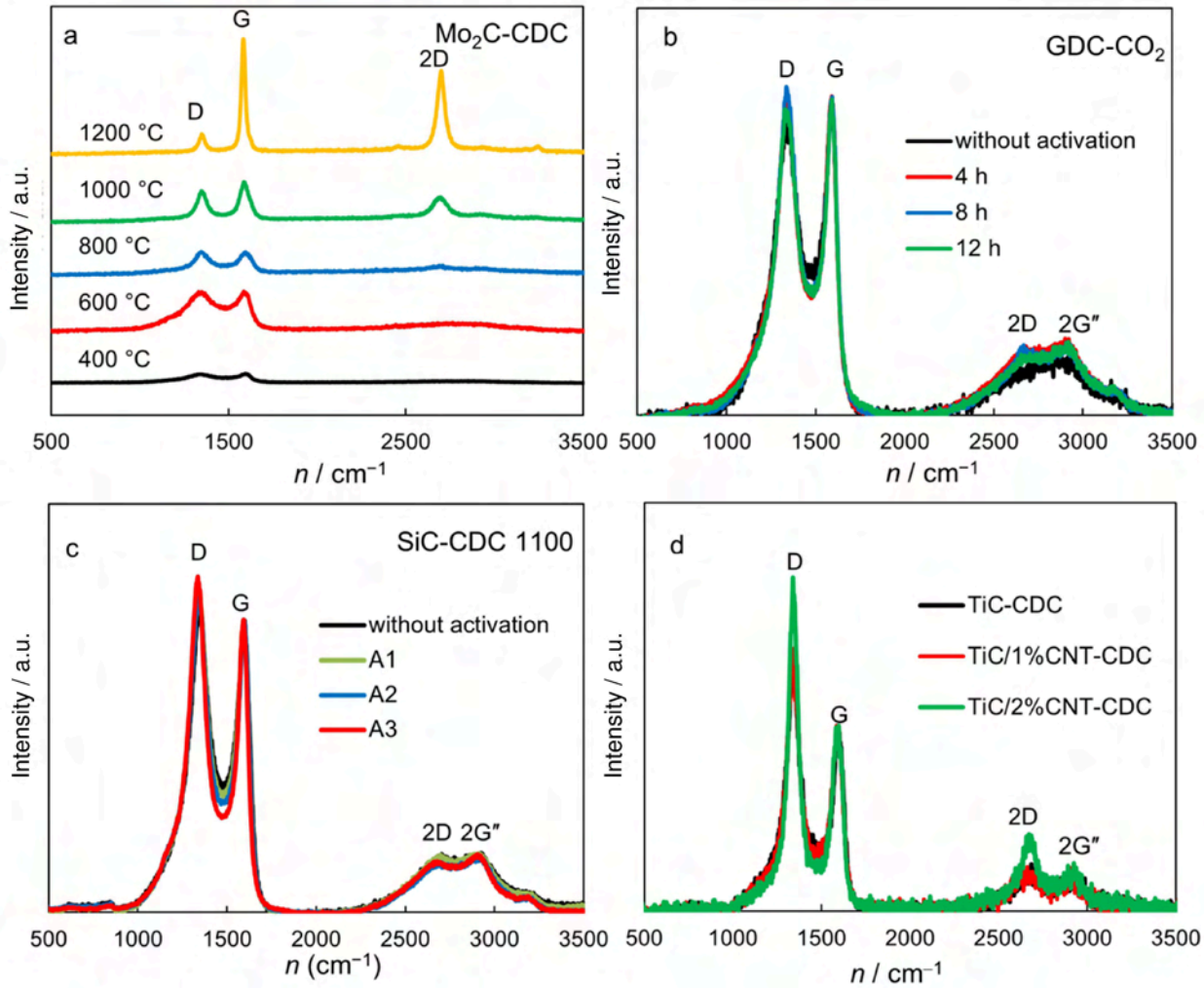
a
Mo2C-CDC
G
2D
D
1200 °C
1000 °C
800 °C
600 °C
400 °C
Intensity / a.u.
500
1500
2500
3500
n / cm−1
b
GDC-CO2
D
G
without activation
4 h
8 h
12 h
2D
2G″
Intensity / a.u.
500
1000
1500
2000
2500
3000
3500
n / cm−1
c
SiC-CDC 1100
D
G
without activation
A1
A2
A3
2D
2G″
Intensity / a.u.
500
1000
1500
2000
2500
3000
3500
n (cm−1)
d
D
G
TiC-CDC
TiC/1%CNT-CDC
TiC/2%CNT-CDC
2D
2G″
Intensity / a.u.
500
1000
1500
2000
2500
3000
3500
n / cm−1

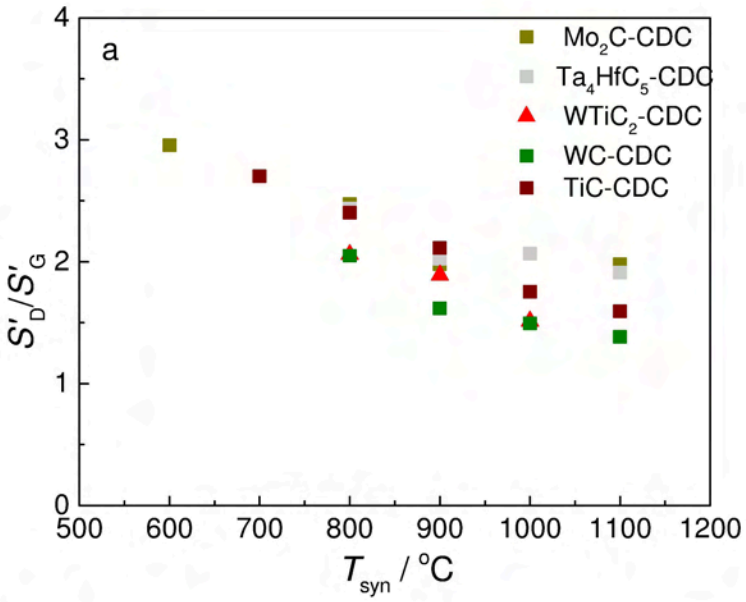
a
Mo2C-CDC
Ta4HfC5-CDC
WTiC2-CDC
WC-CDC
TiC-CDC
S'D/S'G
Tsyn / °C
0
1
2
3
4
500
600
700
800
900
1000
1100
1200

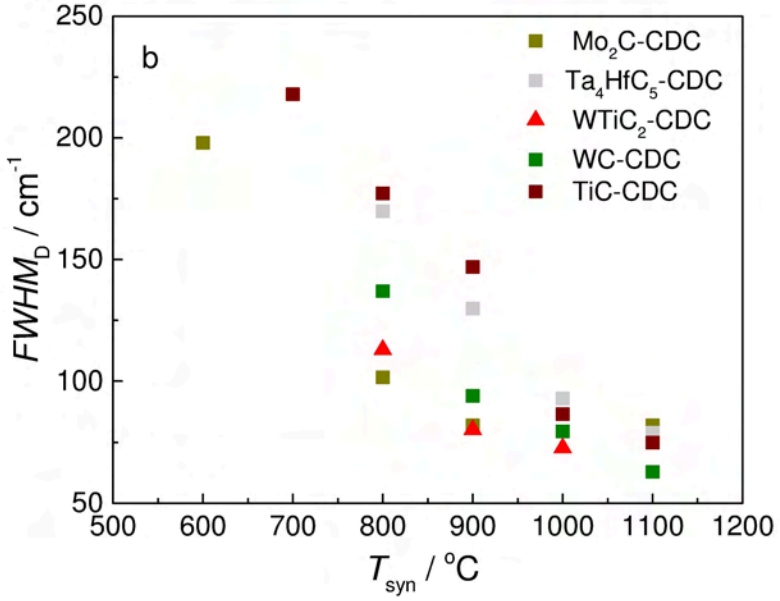
b
Mo2C-CDC
Ta4HfC5-CDC
WTiC2-CDC
WC-CDC
TiC-CDC
FWHMD / cm-1
Tsyn / °C
50
100
150
200
250
500
600
700
800
900
1000
1100
1200

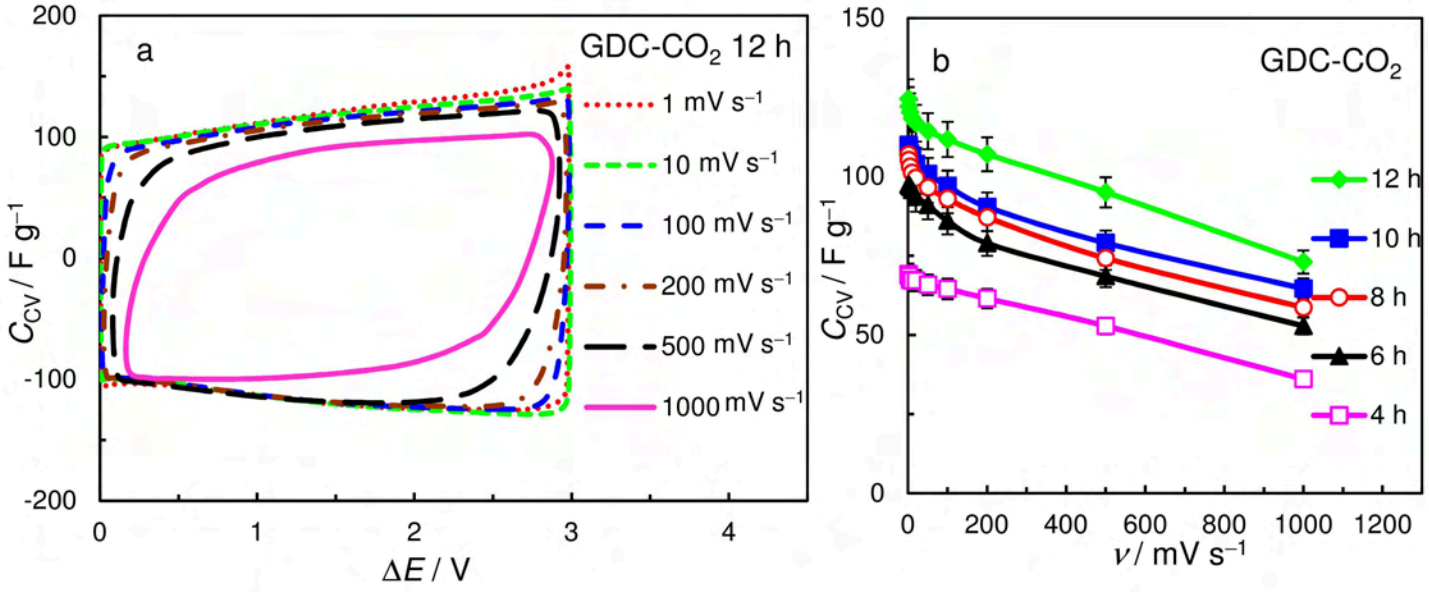
a
GDC-CO2 12 h
1 mV s−1
10 mV s−1
100 mV s−1
200 mV s−1
500 mV s−1
1000 mV s−1
CCV / F g−1
ΔE / V
200
100
0
-100
-200
0
1
2
3
4
b
GDC-CO2
12 h
10 h
8 h
6 h
4 h
CCV / F g−1
ν / mV s−1
150
100
50
0
0
200
400
600
800
1000
1200

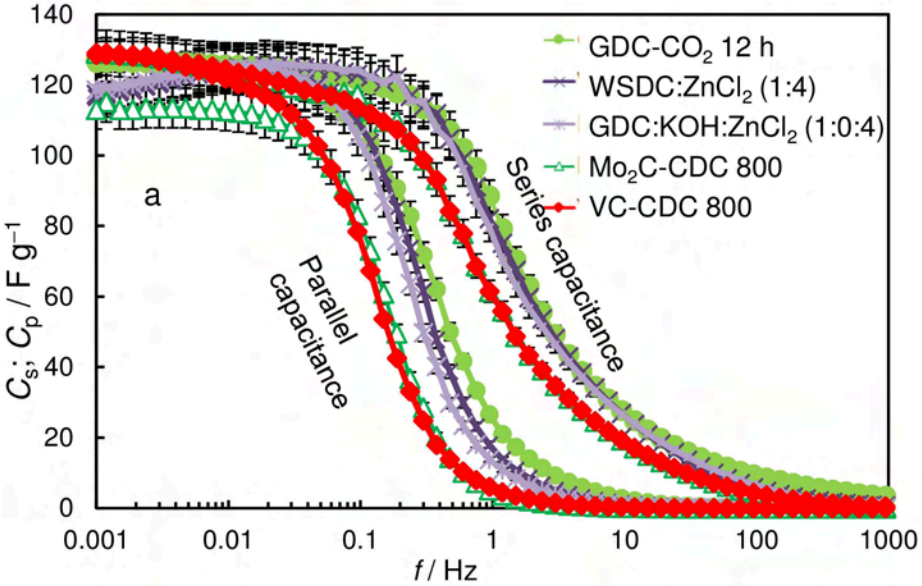
a
GDC-CO2 12 h
WSDC:ZnCl2 (1:4)
GDC:KOH:ZnCl2 (1:0:4)
Mo2C-CDC 800
VC-CDC 800
Series capacitance
Parallel capacitance
Cs; Cp / F g−1
f / Hz
0
20
40
60
80
100
120
140
0.001
0.01
0.1
1
10
100
1000

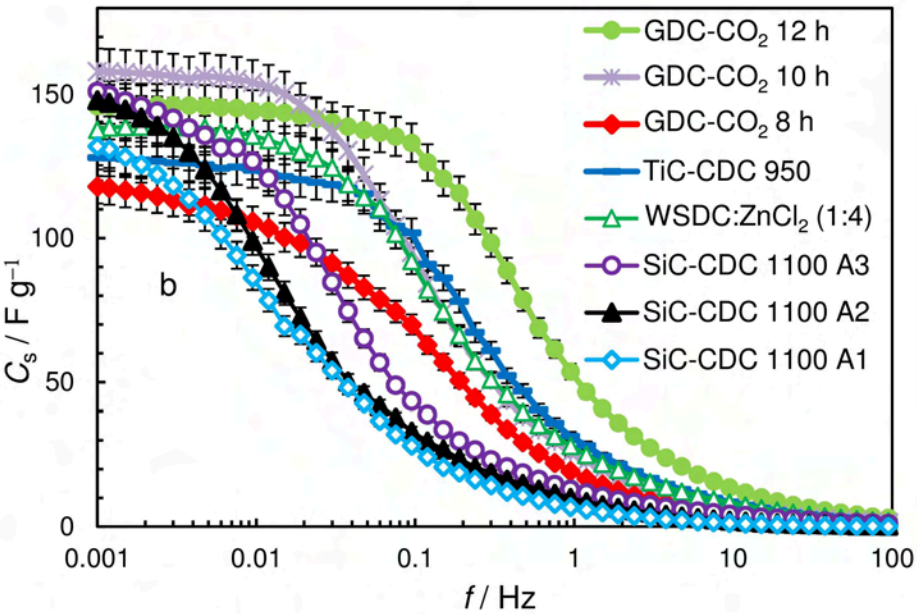
b
GDC-CO2 12 h
GDC-CO2 10 h
GDC-CO2 8 h
TiC-CDC 950
WSDC:ZnCl2 (1:4)
SiC-CDC 1100 A3
SiC-CDC 1100 A2
SiC-CDC 1100 A1
Cs / F g−1
f / Hz
0
50
100
150
0.001
0.01
0.1
1
10
100

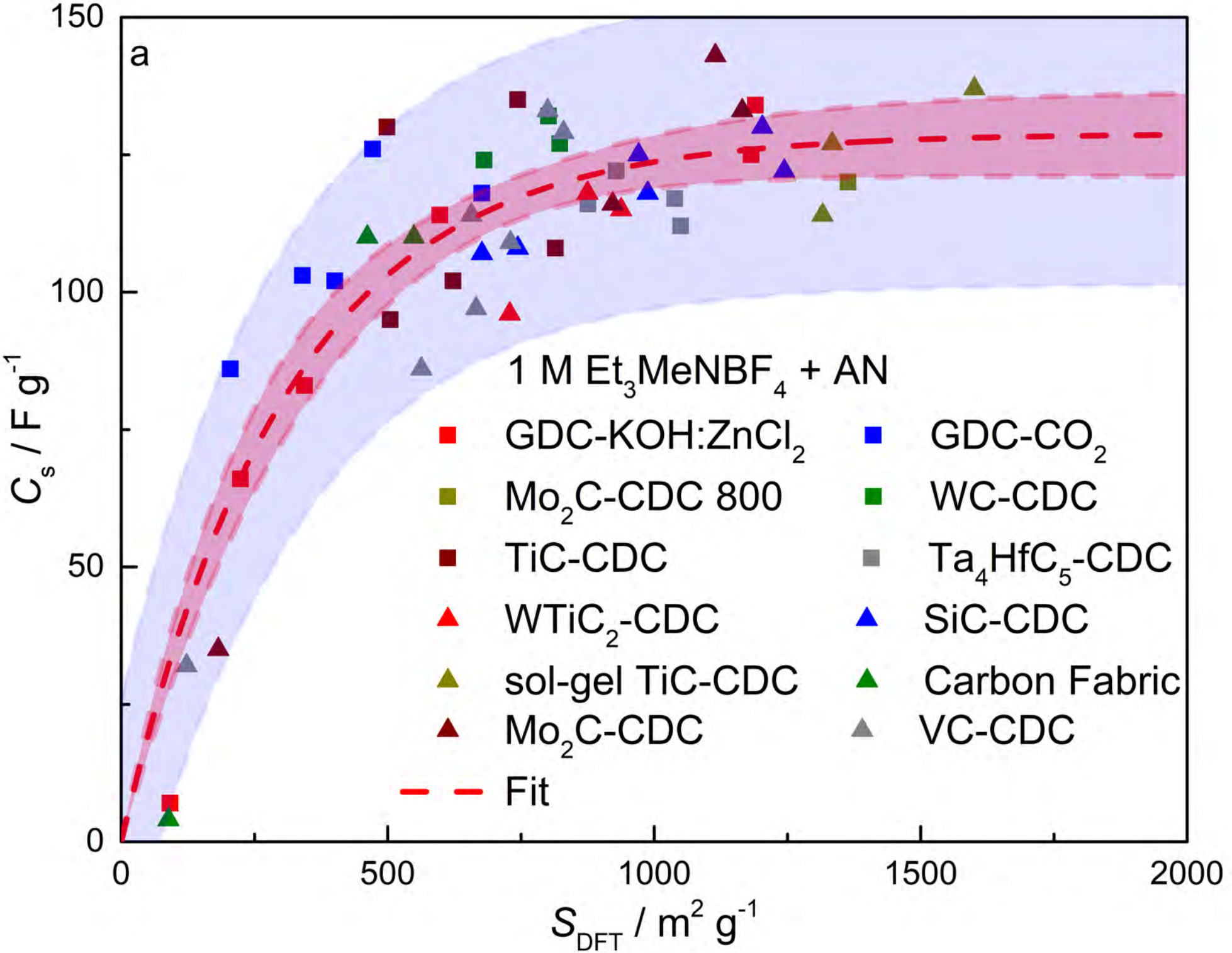
a
1 M Et3MeNBF4 + AN
GDC-KOH:ZnCl2
GDC-CO2
Mo2C-CDC 800
WC-CDC
TiC-CDC
Ta4HfC5-CDC
WTiC2-CDC
SiC-CDC
sol-gel TiC-CDC
Carbon Fabric
Mo2C-CDC
VC-CDC
Fit
Cs / F g-1
SDFT / m2 g-1
0
50
100
150
0
500
1000
1500
2000

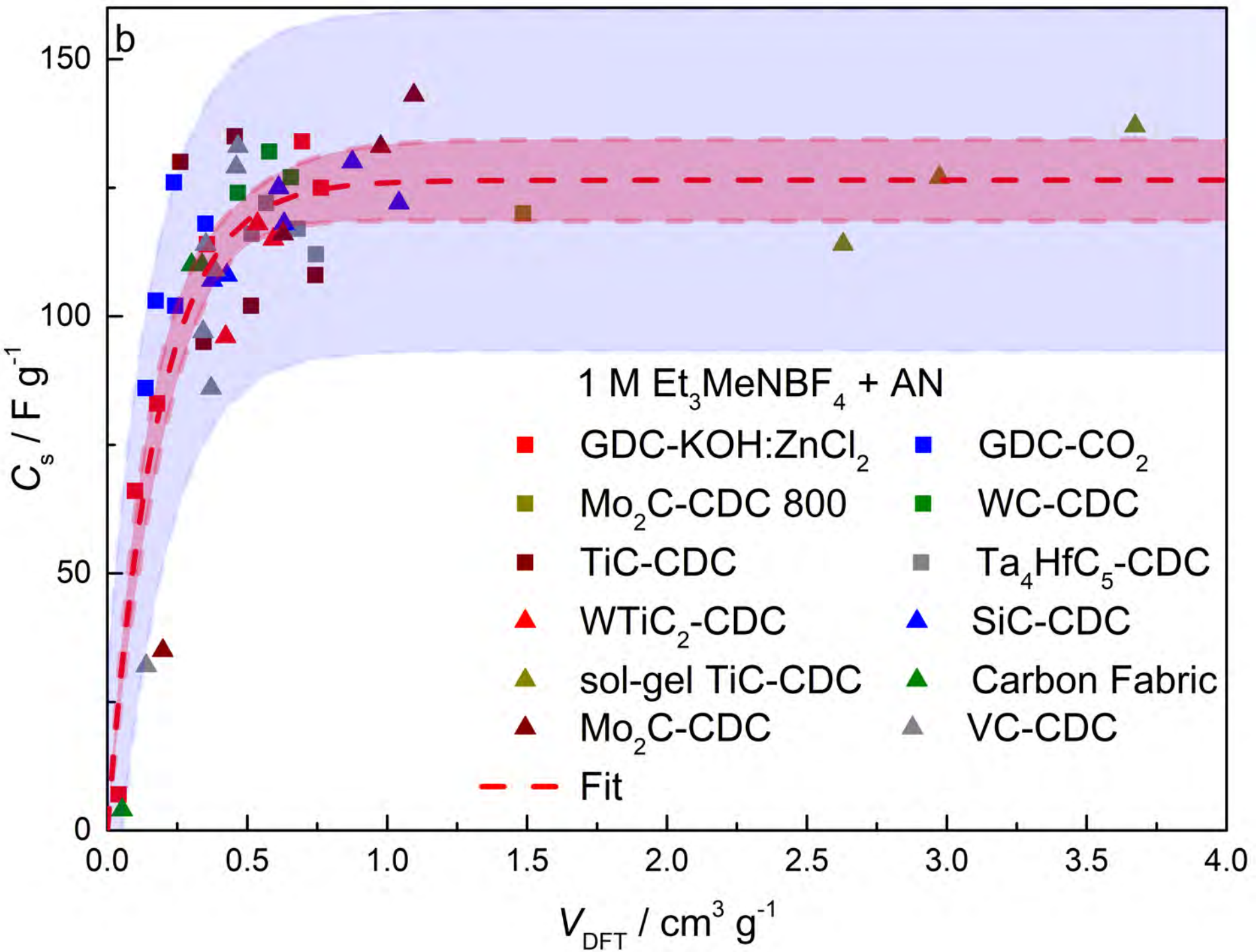
b
150
100
50
0
0.0
0.5
1.0
1.5
2.0
2.5
3.0
3.5
4.0
C_s / F g^{-1}
V_{DFT} / cm^3 g^{-1}
1 M Et_3MeNBF_4 + AN
GDC-KOH:$ZnCl_2$
GDC-CO_2
Mo_2C-CDC 800
WC-CDC
TiC-CDC
Ta_4HfC_5-CDC
$WTiC_2$-CDC
SiC-CDC
sol-gel TiC-CDC
Carbon Fabric
Mo_2C-CDC
VC-CDC
Fit

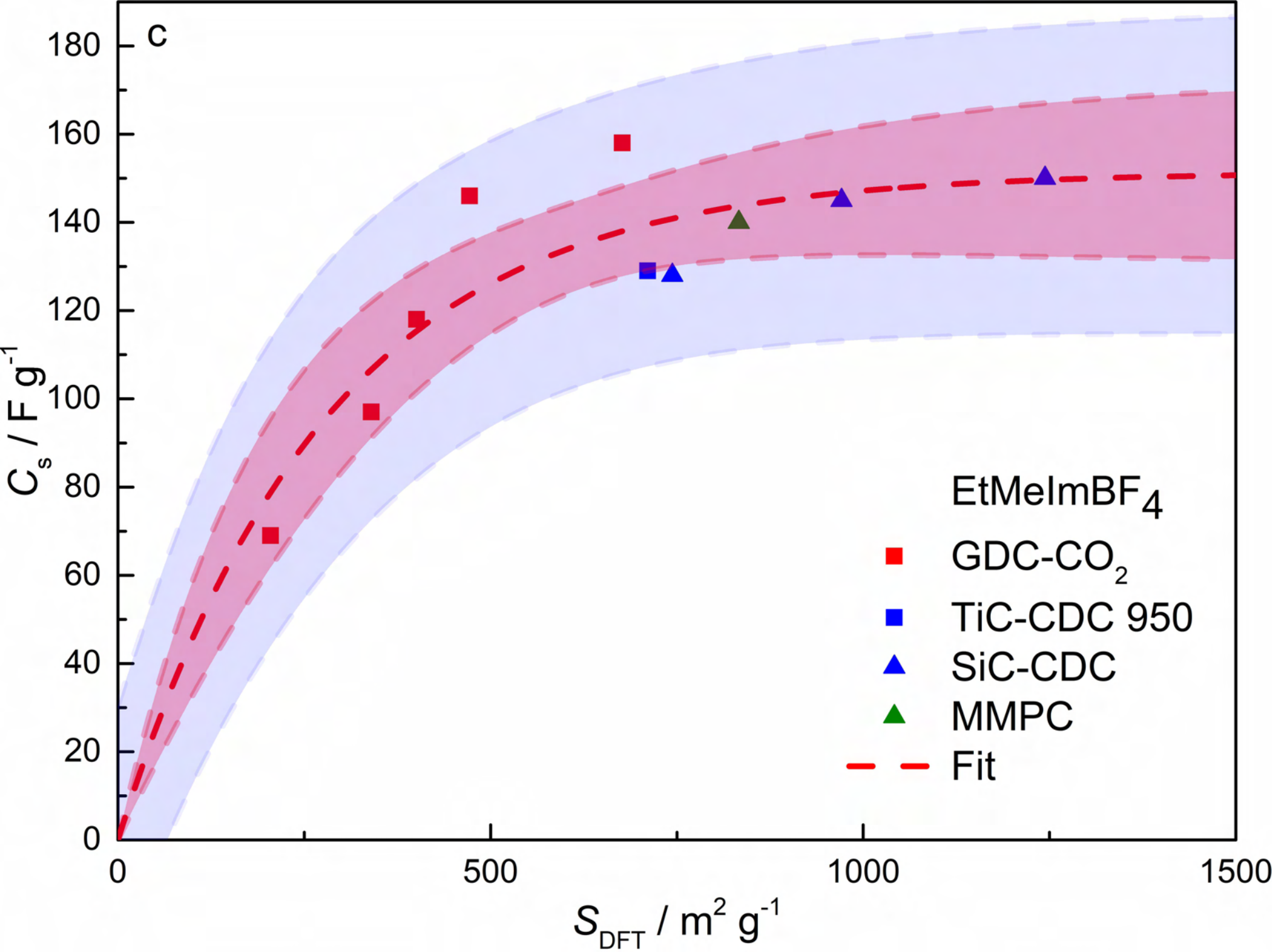
c
180
160
140
120
100
80
60
40
20
0
C_s / F g^{-1}
0
500
1000
1500
S_{DFT} / m^2 g^{-1}
EtMeImBF$_4$
GDC-CO$_2$
TiC-CDC 950
SiC-CDC
MMPC
Fit

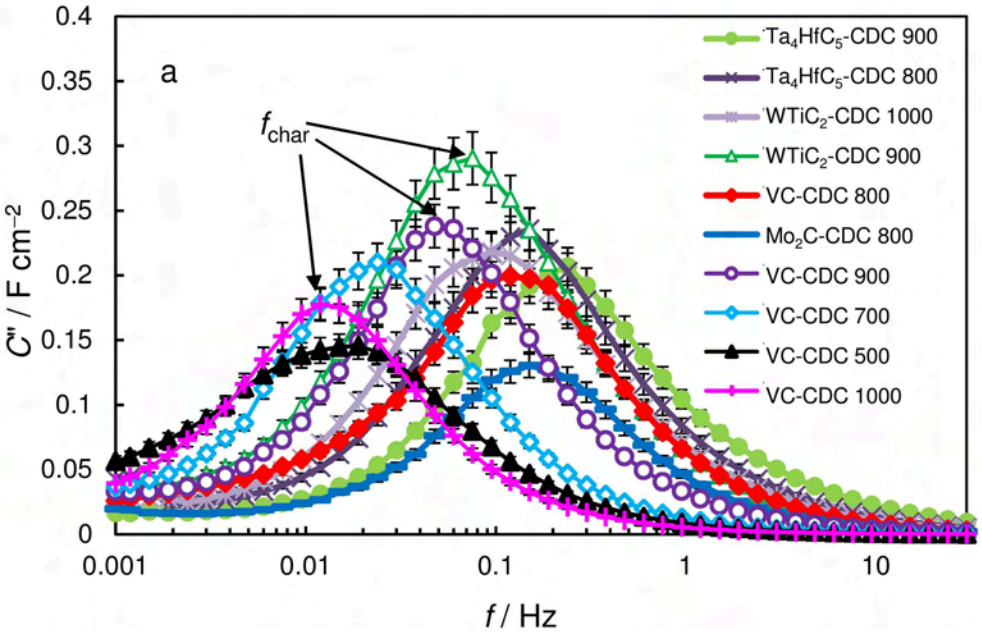
a
f_{char}
Ta_4HfC_5-CDC 900
Ta_4HfC_5-CDC 800
$WTiC_2$-CDC 1000
$WTiC_2$-CDC 900
VC-CDC 800
Mo_2C-CDC 800
VC-CDC 900
VC-CDC 700
VC-CDC 500
VC-CDC 1000
C'' / F cm^{-2}
f / Hz
0.4
0.35
0.3
0.25
0.2
0.15
0.1
0.05
0
0.001
0.01
0.1
1
10

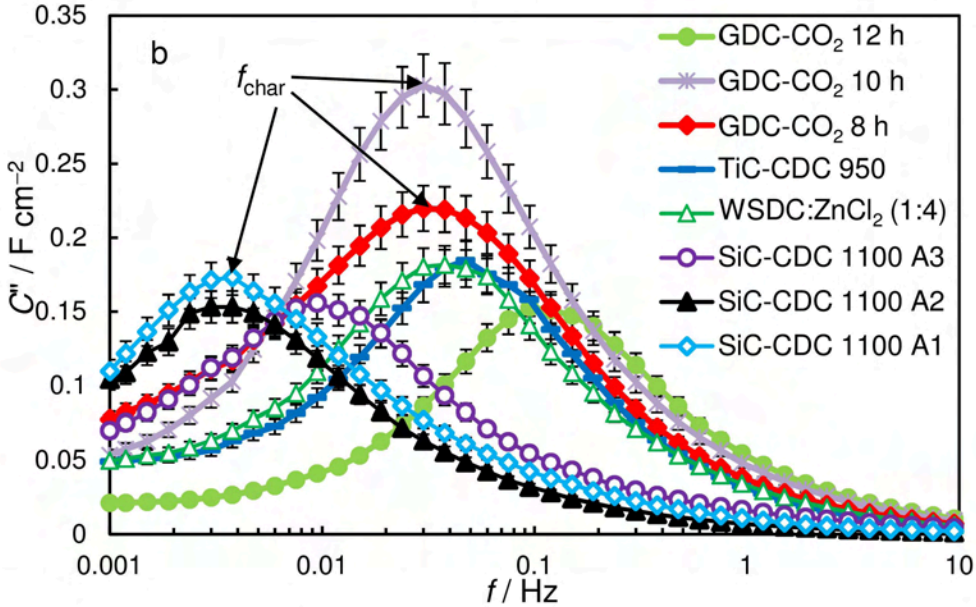
b
f_{char}
GDC-CO_2 12 h
GDC-CO_2 10 h
GDC-CO_2 8 h
TiC-CDC 950
WSDC:$ZnCl_2$ (1:4)
SiC-CDC 1100 A3
SiC-CDC 1100 A2
SiC-CDC 1100 A1
C'' / F cm^{-2}
f / Hz
0.35
0.3
0.25
0.2
0.15
0.1
0.05
0
0.001
0.01
0.1
1
10

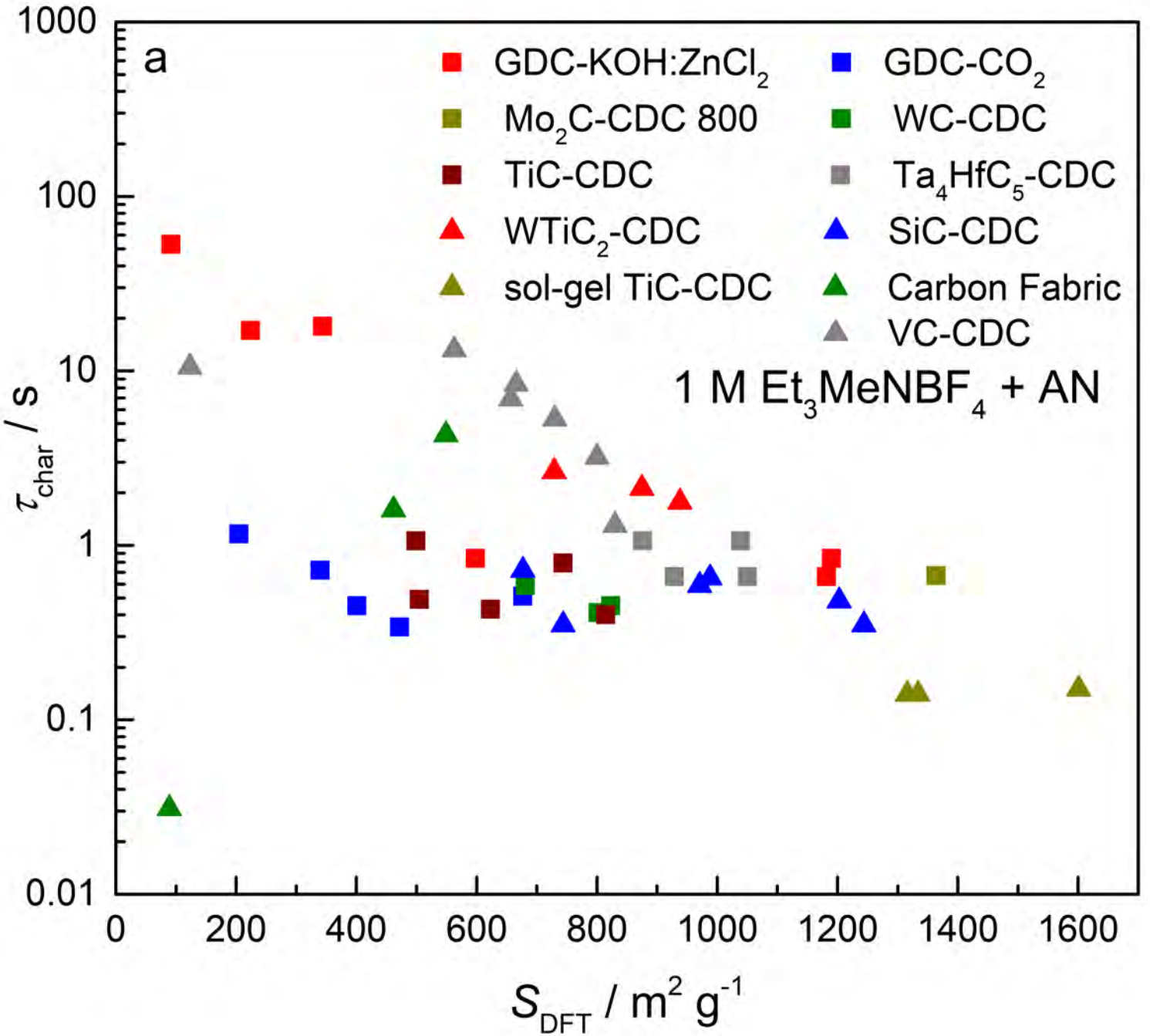
a
GDC-KOH:ZnCl2
GDC-CO2
Mo2C-CDC 800
WC-CDC
TiC-CDC
Ta4HfC5-CDC
WTiC2-CDC
SiC-CDC
sol-gel TiC-CDC
Carbon Fabric
VC-CDC
1 M Et3MeNBF4 + AN
τchar / s
SDFT / m2 g-1
1000
100
10
1
0.1
0.01
0
200
400
600
800
1000
1200
1400
1600

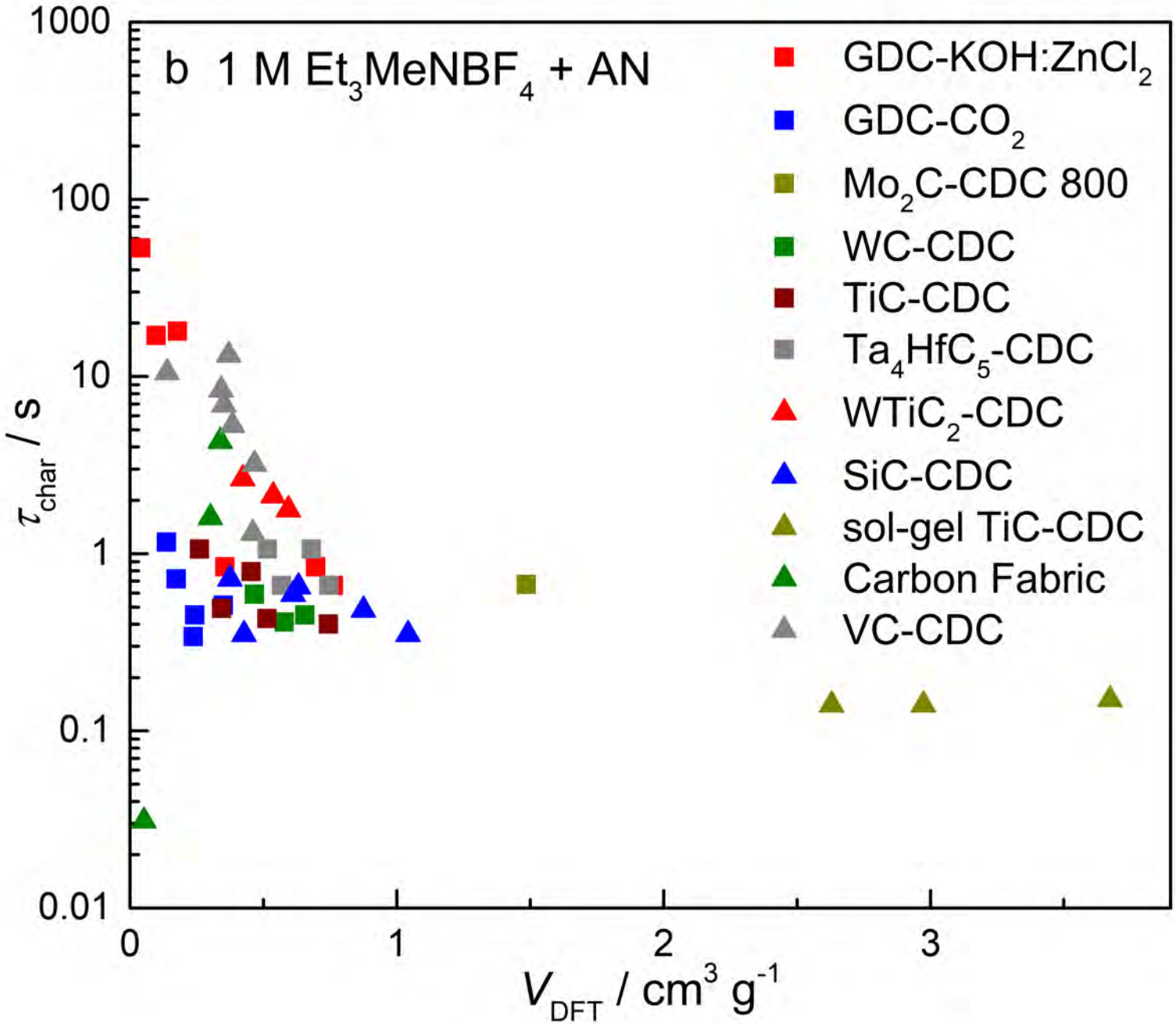
b 1 M Et3MeNBF4 + AN
GDC-KOH:ZnCl2
GDC-CO2
Mo2C-CDC 800
WC-CDC
TiC-CDC
Ta4HfC5-CDC
WTiC2-CDC
SiC-CDC
sol-gel TiC-CDC
Carbon Fabric
VC-CDC
τchar / s
VDFT / cm3 g-1
1000
100
10
1
0.1
0.01
0
1
2
3

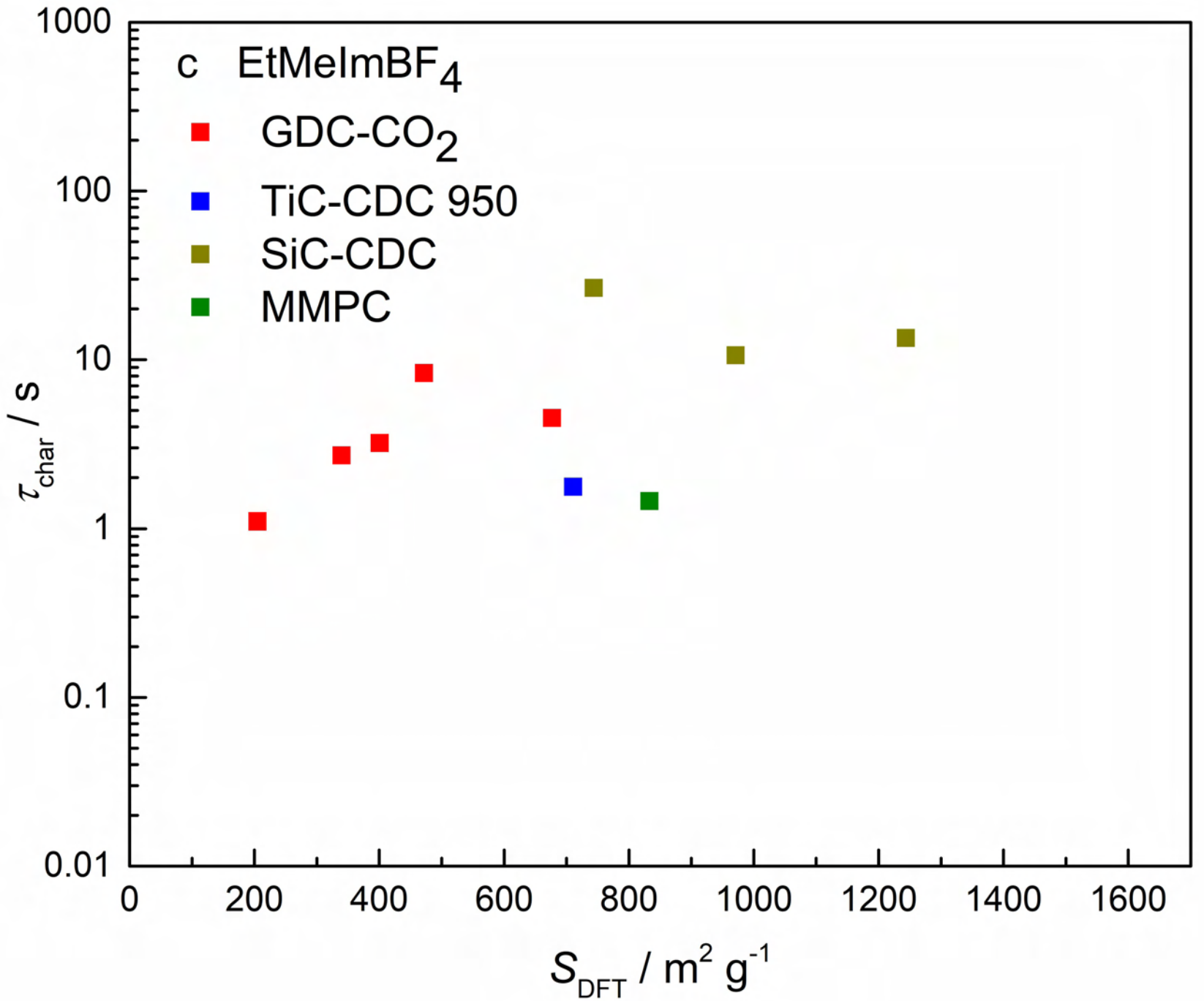
c EtMeImBF4
GDC-CO2
TiC-CDC 950
SiC-CDC
MMPC
1000
100
10
1
0.1
0.01
τchar / s
0
200
400
600
800
1000
1200
1400
1600
SDFT / m2 g-1

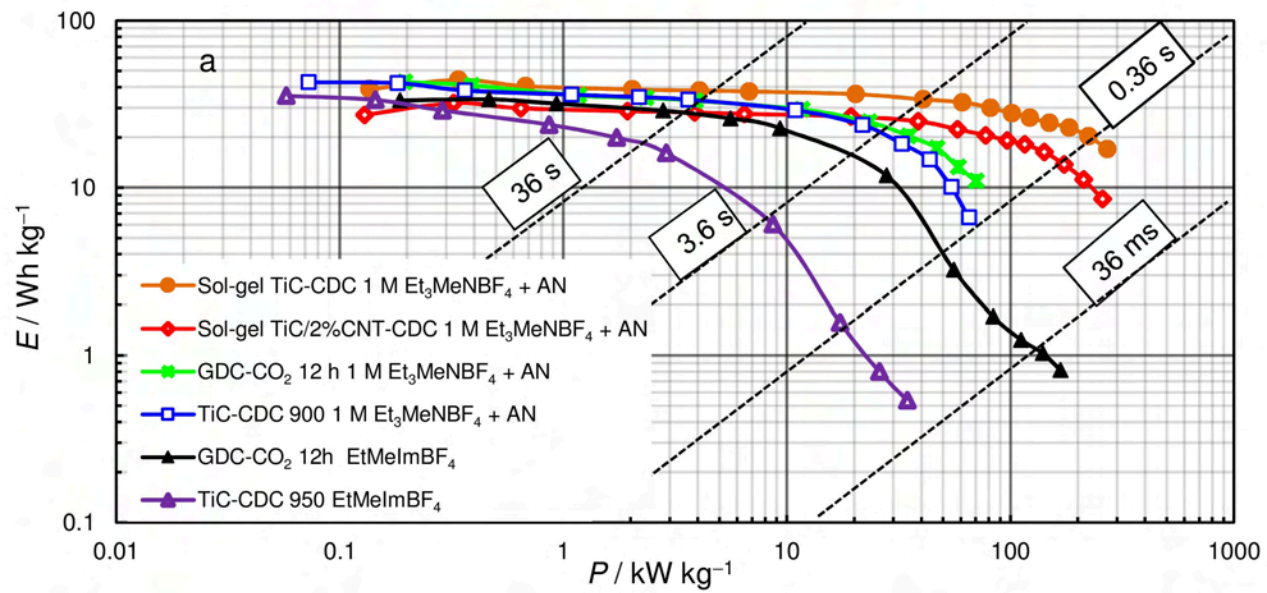
a
0.36 s
36 s
3.6 s
36 ms
Sol-gel TiC-CDC 1 M Et3MeNBF4 + AN
Sol-gel TiC/2%CNT-CDC 1 M Et3MeNBF4 + AN
GDC-CO2 12 h 1 M Et3MeNBF4 + AN
TiC-CDC 900 1 M Et3MeNBF4 + AN
GDC-CO2 12h EtMeImBF4
TiC-CDC 950 EtMeImBF4
E / Wh kg−1
P / kW kg−1
100
10
1
0.1
0.01
0.1
1
10
100
1000

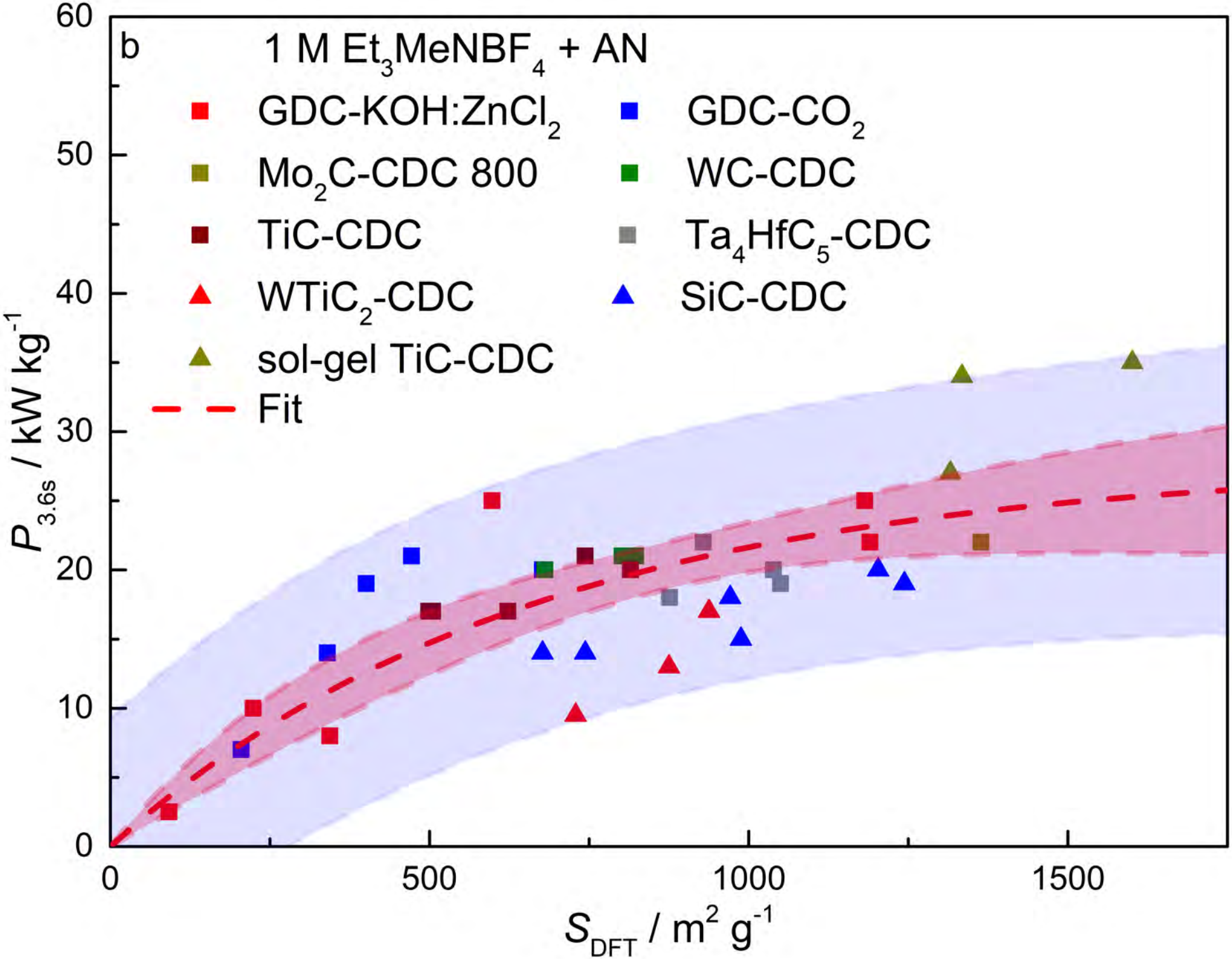
b
1 M Et3MeNBF4 + AN
GDC-KOH:ZnCl2
GDC-CO2
Mo2C-CDC 800
WC-CDC
TiC-CDC
Ta4HfC5-CDC
WTiC2-CDC
SiC-CDC
sol-gel TiC-CDC
Fit
P3.6s / kW kg-1
SDFT / m2 g-1
0
10
20
30
40
50
60
0
500
1000
1500

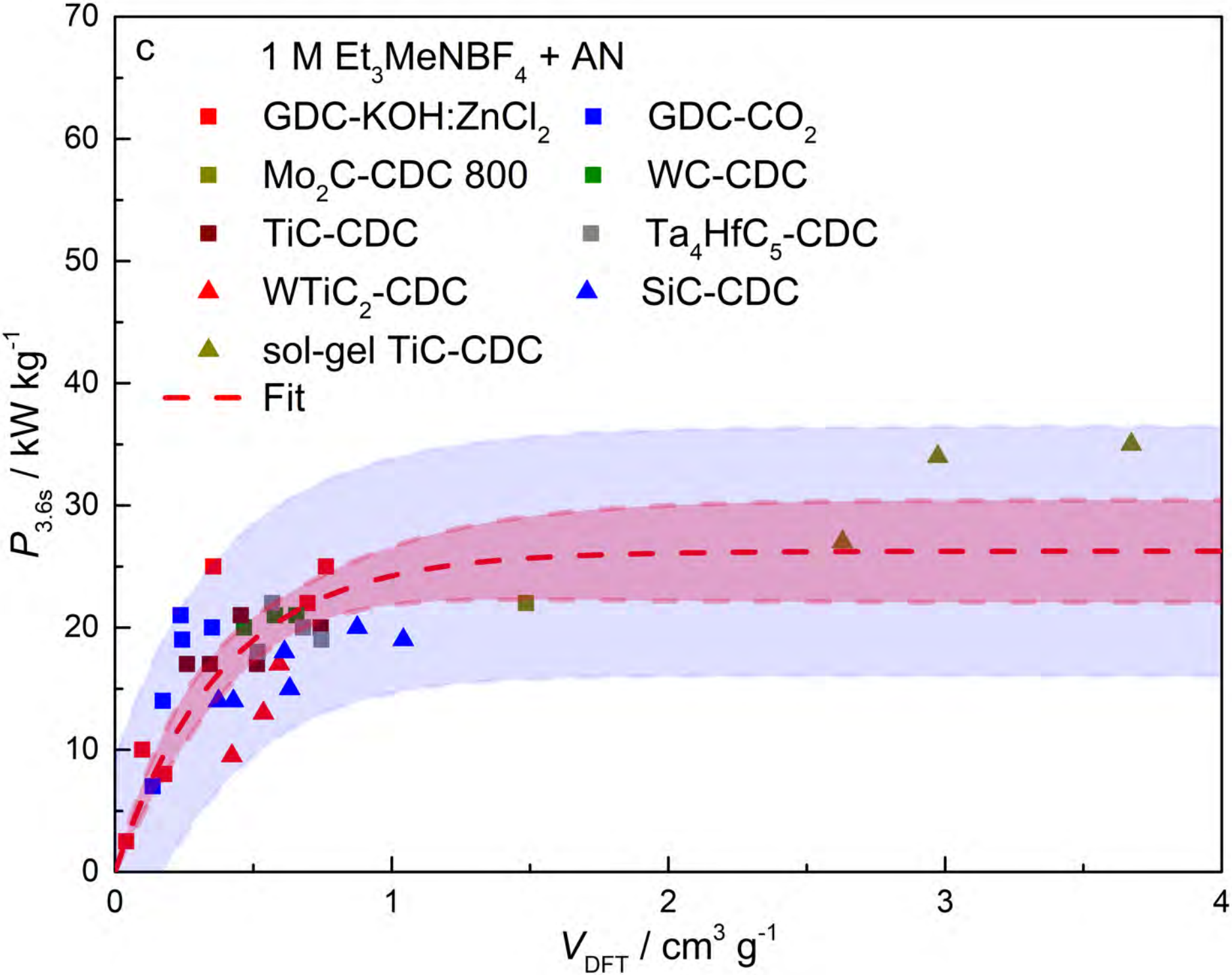
c
1 M Et3MeNBF4 + AN
GDC-KOH:ZnCl2
GDC-CO2
Mo2C-CDC 800
WC-CDC
TiC-CDC
Ta4HfC5-CDC
WTiC2-CDC
SiC-CDC
sol-gel TiC-CDC
Fit
P3.6s / kW kg-1
VDFT / cm3 g-1
0
10
20
30
40
50
60
70
0
1
2
3
4

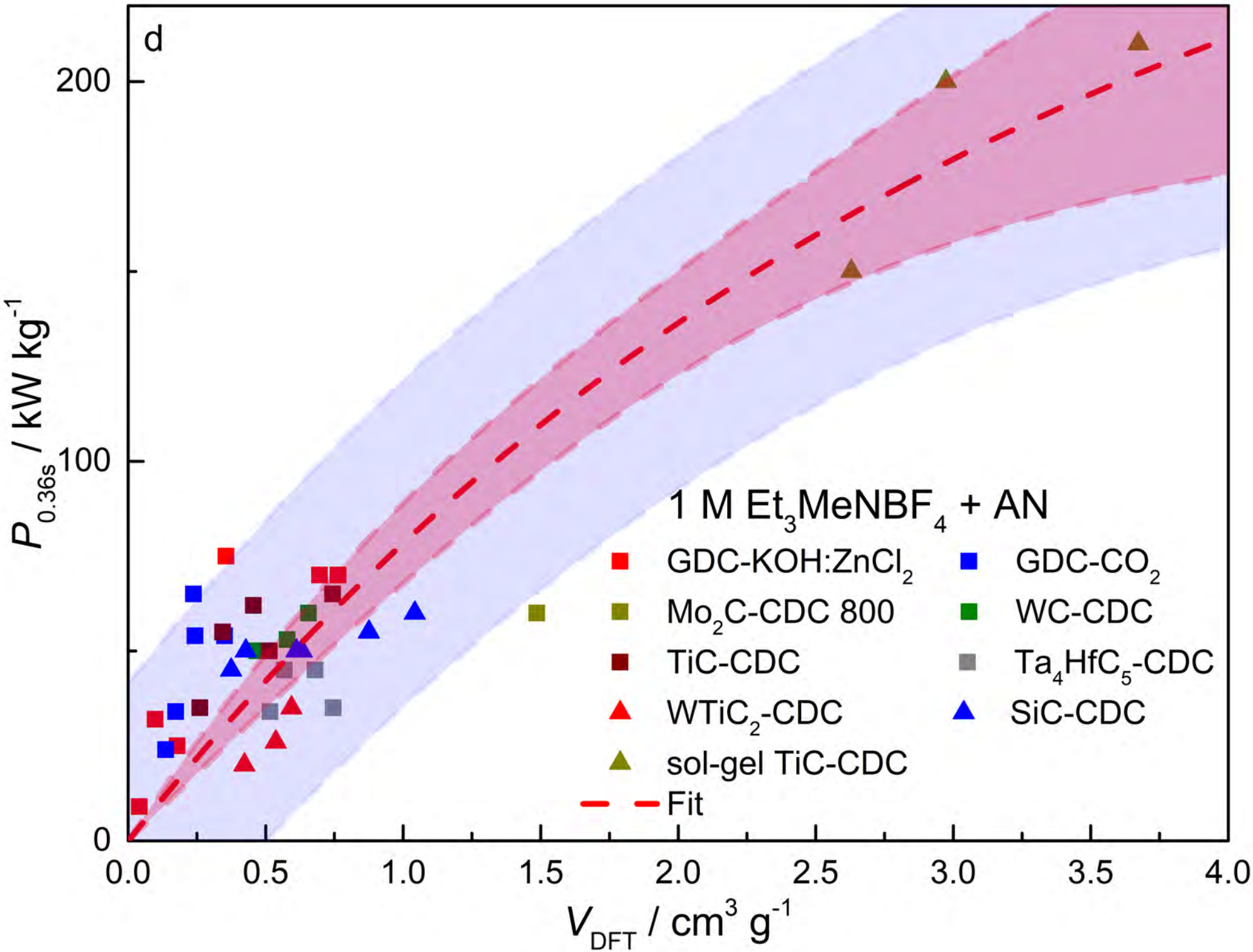
d
1 M Et3MeNBF4 + AN
GDC-KOH:ZnCl2
GDC-CO2
Mo2C-CDC 800
WC-CDC
TiC-CDC
Ta4HfC5-CDC
WTiC2-CDC
SiC-CDC
sol-gel TiC-CDC
Fit
P0.36s / kW kg-1
VDFT / cm3 g-1
0
100
200
0.0
0.5
1.0
1.5
2.0
2.5
3.0
3.5
4.0

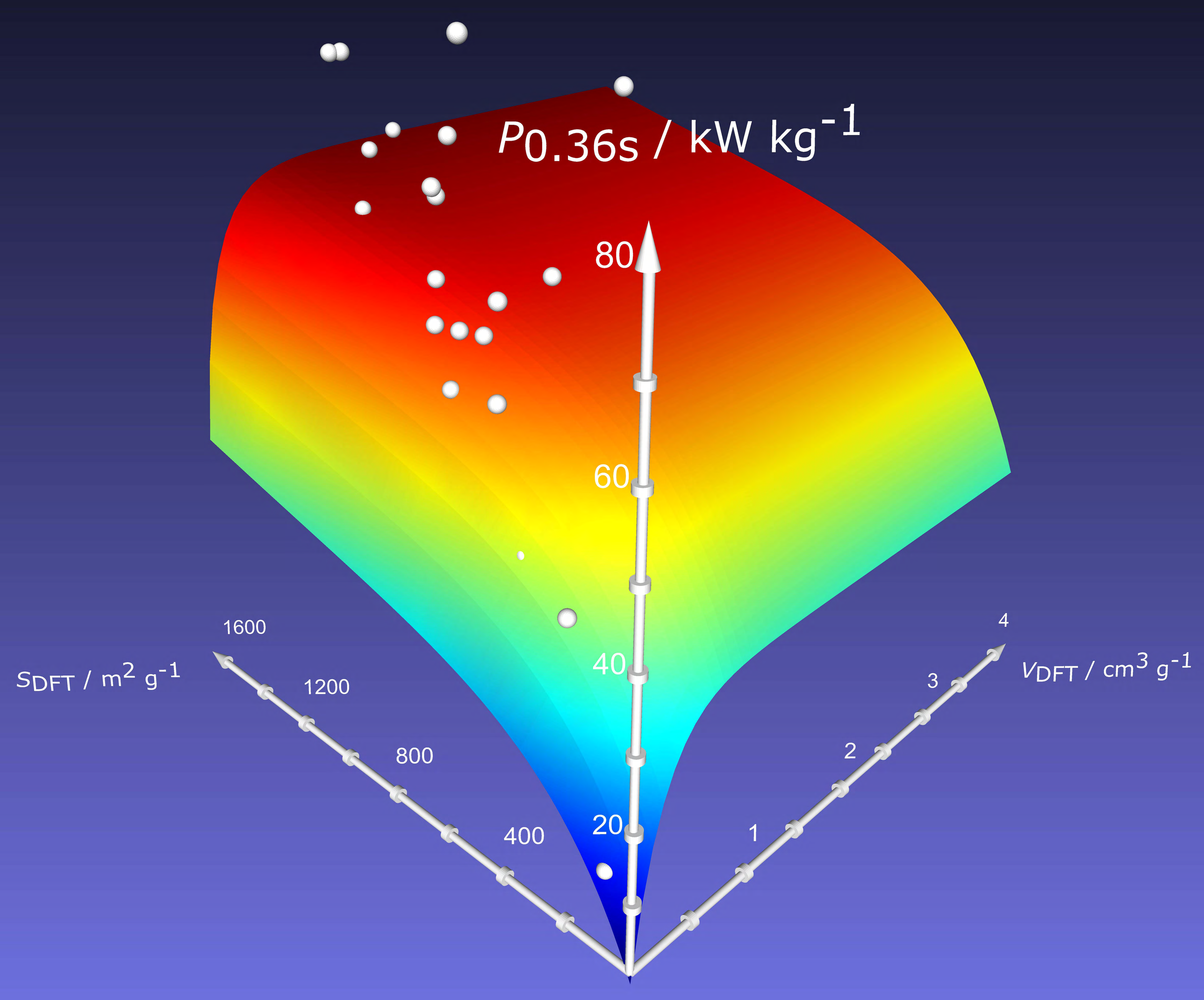
P0.36s / kW kg-1
80
60
40
20
SDFT / m2 g-1
1600
1200
800
400
VDFT / cm3 g-1
4
3
2
1

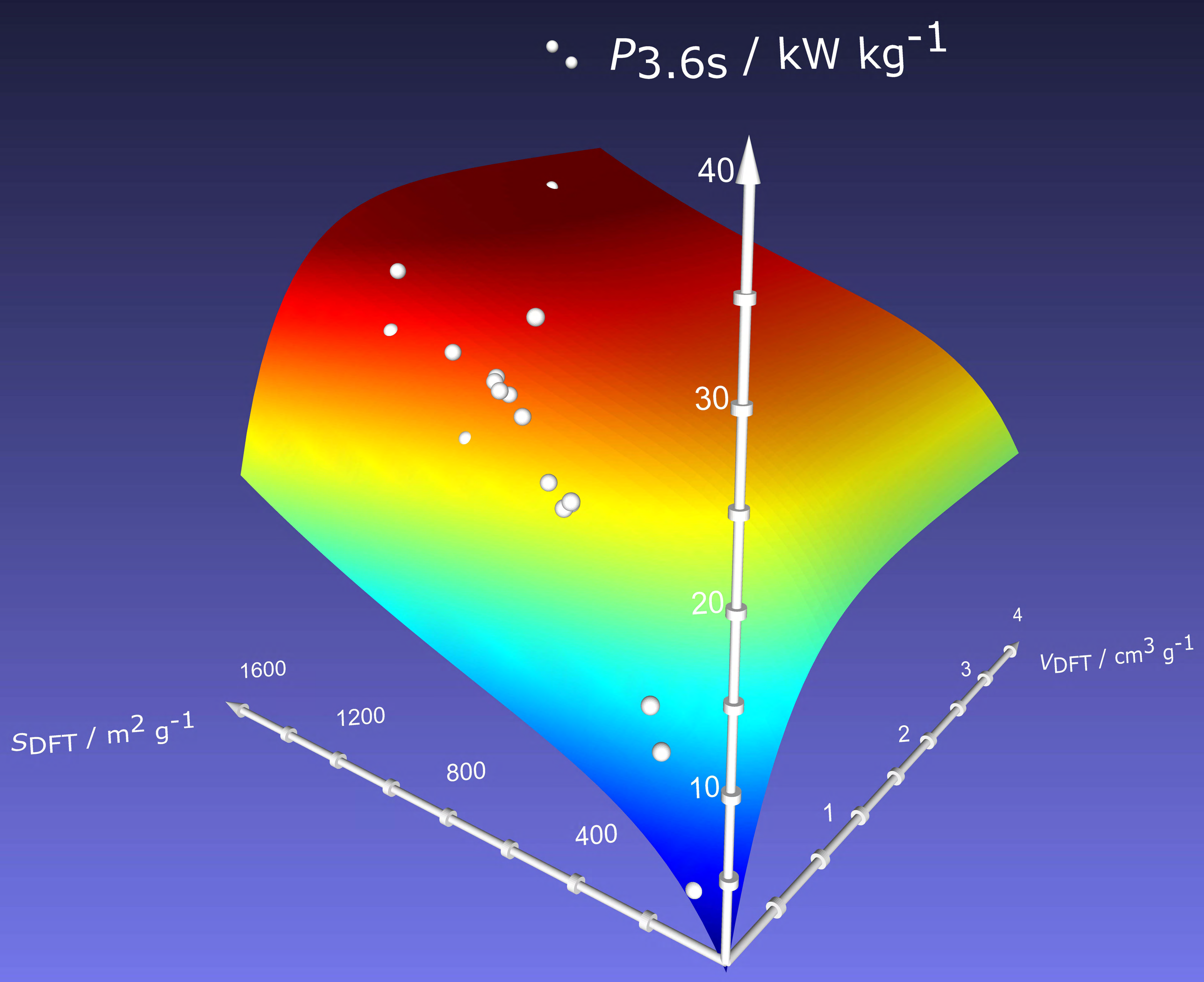
P3.6s / kW kg-1
40
30
20
10
1600
1200
800
400
SDFT / m2 g-1
4
3
2
1
VDFT / cm3 g-1

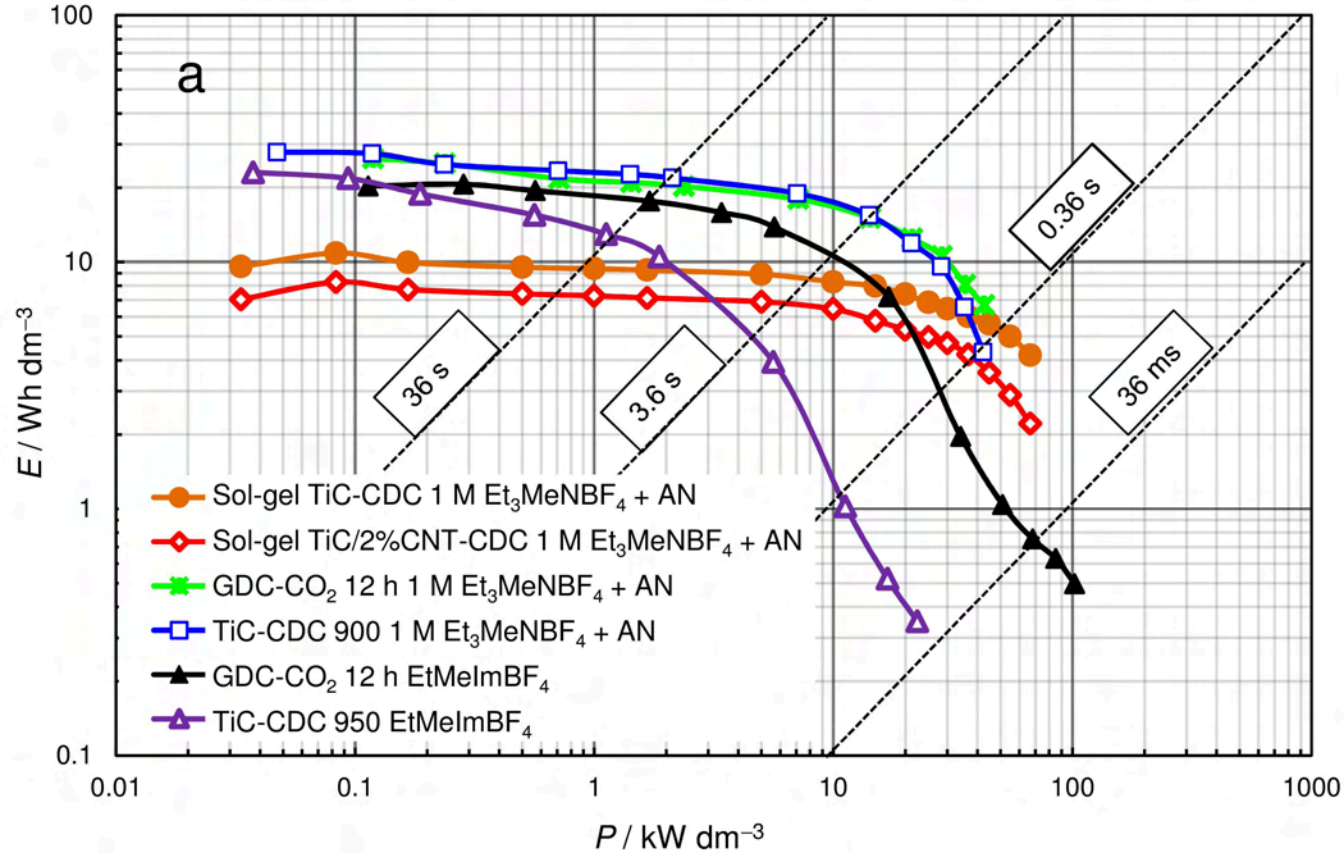
a
100
10
1
0.1
0.01
0.1
1
10
100
1000
E / Wh dm−3
P / kW dm−3
36 s
3.6 s
0.36 s
36 ms
Sol-gel TiC-CDC 1 M Et3MeNBF4 + AN
Sol-gel TiC/2%CNT-CDC 1 M Et3MeNBF4 + AN
GDC-CO2 12 h 1 M Et3MeNBF4 + AN
TiC-CDC 900 1 M Et3MeNBF4 + AN
GDC-CO2 12 h EtMeImBF4
TiC-CDC 950 EtMeImBF4

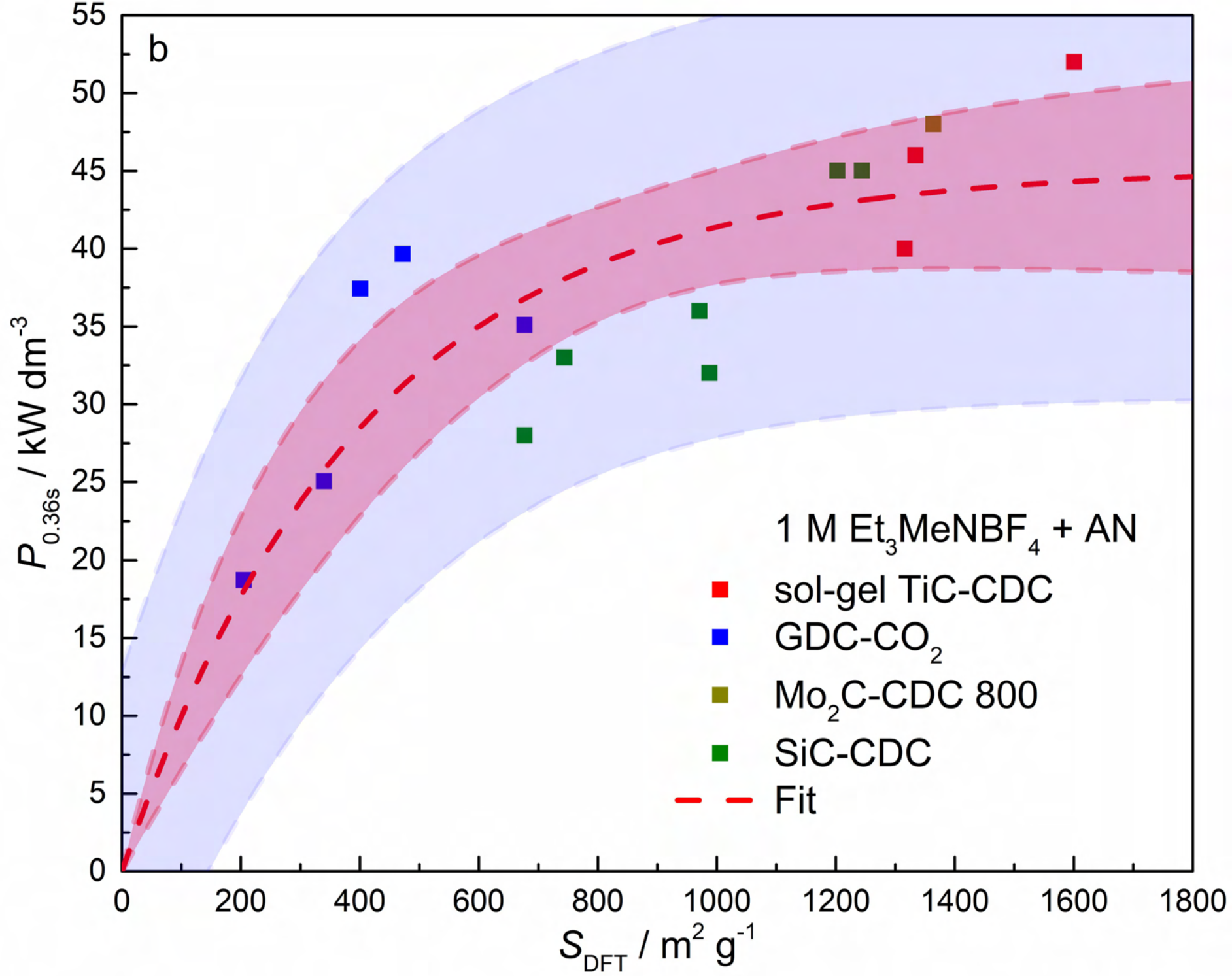
b
1 M Et3MeNBF4 + AN
sol-gel TiC-CDC
GDC-CO2
Mo2C-CDC 800
SiC-CDC
Fit
P0.36s / kW dm-3
SDFT / m2 g-1
0
5
10
15
20
25
30
35
40
45
50
55
0
200
400
600
800
1000
1200
1400
1600
1800

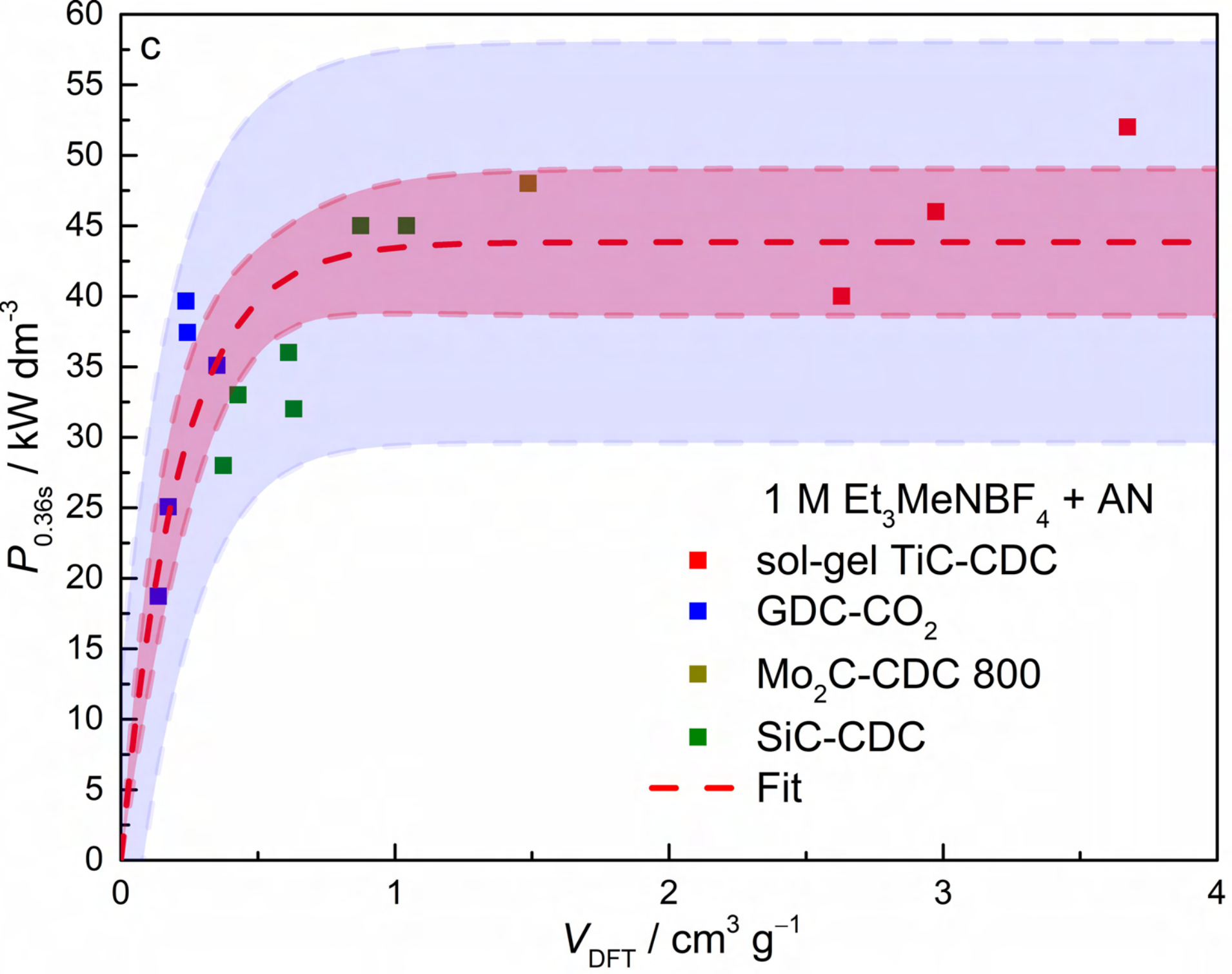
c
1 M Et3MeNBF4 + AN
sol-gel TiC-CDC
GDC-CO2
Mo2C-CDC 800
SiC-CDC
Fit
P0.36s / kW dm-3
VDFT / cm3 g-1
0
5
10
15
20
25
30
35
40
45
50
55
60
0
1
2
3
4

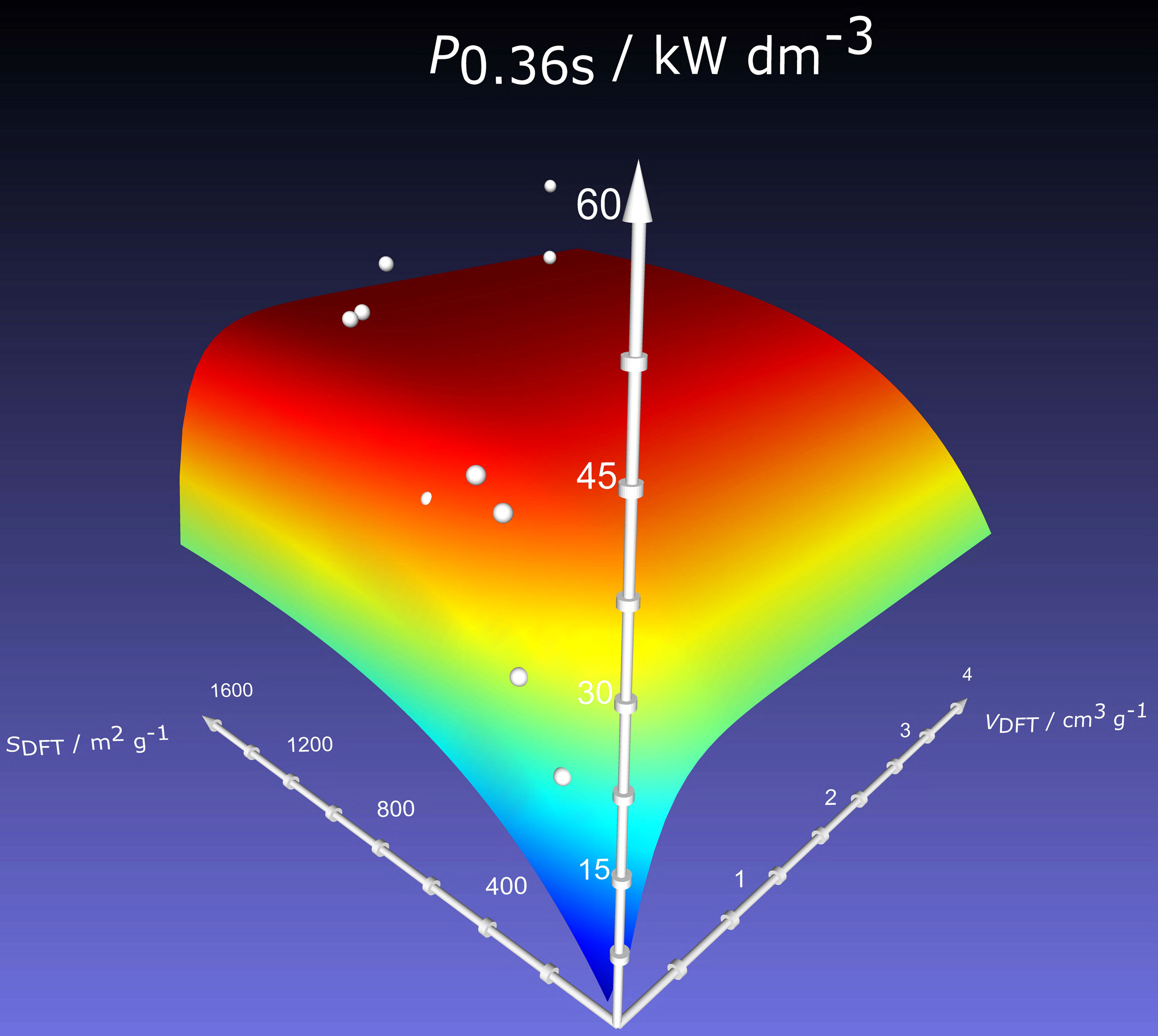
P0.36s / kW dm-3
60
45
30
15
1600
1200
800
400
SDFT / m2 g-1
4
3
2
1
VDFT / cm3 g-1

ACCEPTED MANUSCRIPT

Highlights

- Series capacitance scale up to limiting values at high surface area values
- Energy and power densities scale up to limiting values at high surface area values
- High mesoporosity of materials enables high energy and power densities
- Pore size distribution depends on the pore geometry assumed
- Ultramicropores cannot be applied for quick energy storage

ACCEPTED MANUSCRIPT

ACCEPTED MANUSCRIPT

Data visualization description:

Two software packages were used for creating 3D models (Fig. 15e 3D; Fig. 15f 3D and Fig. 16d 3D). MeshLab 2016.12 was used for creating a color mapped surface from the calculated point cloud and Blender 2.79b was used for creating UV spheres from experimental data point cloud and creating axes with labels.

Files upload description:

Fig. 15e 3D.zip

This zip-file contains 3 u3d 3D models:

1. The modeled 3D surface, which should be color mapped according to Z-axis value. Please see file Fig. 15e.tif for reference.

2. The experimental data points, modeled as spheres

3. The axes and labels as I do not know whether the 3D viewer would provide axes and labels.

Fig. 15f 3D.zip

This zip-file contains 3 u3d 3D models:

1. The modeled 3D surface, which should be color mapped according to Z-axis value. Please see file Fig. 15f.tif for reference.

2. The experimental data points, modeled as spheres

3. The axes and labels as I do not know whether the 3D viewer would provide axes and labels.

Fig. 16d 3D.zip

This zip-file contains 3 u3d 3D models:

1. The modeled 3D surface, which should be color mapped according to Z-axis value. Please see file Fig. 16d.tif for reference.

2. The experimental data points, modeled as spheres

3. The axes and labels as I do not know whether the 3D viewer would provide axes and labels.

ACCEPTED MANUSCRIPT